

# Graphene Nanoribbons: On-Surface Synthesis and Integration into Electronic Devices

Zongping Chen,\* Akimitsu Narita,\* and Klaus Müllen\*

Graphene nanoribbons (GNRs) are quasi-1D graphene strips, which have attracted attention as a novel class of semiconducting materials for various applications in electronics and optoelectronics. GNRs exhibit unique electronic and optical properties, which sensitively depend on their chemical structures, especially the width and edge configuration. Therefore, precision synthesis of GNRs with chemically defined structures is crucial for their fundamental studies as well as device applications. In contrast to top-down methods, bottom-up chemical synthesis using tailor-made molecular precursors can achieve atomically precise GNRs. Here, the synthesis of GNRs on metal surfaces under ultrahigh vacuum (UHV) and chemical vapor deposition (CVD) conditions is the main focus, and the recent progress in the field is summarized. The UHV method leads to successful unambiguous visualization of atomically precise structures of various GNRs with different edge configurations. The CVD protocol, in contrast, achieves simpler and industry-viable fabrication of GNRs, allowing for the scale up and efficient integration of the as-grown GNRs into devices. The recent updates in device studies are also addressed using GNRs synthesized by both the UHV method and CVD, mainly for transistor applications. Furthermore, views on the next steps and challenges in the field of on-surface synthesized GNRs are provided.

## 1. Introduction

Graphene, a 2D material consisting of  $sp^2$ -hybridized carbon atoms, has attracted much interest over the years since its first isolation and characterization in 2004.<sup>[1]</sup> Graphene subsequently prompted numerous applications due to its outstanding properties, including high intrinsic charge carrier mobility,<sup>[2]</sup> thermal conductivity,<sup>[3]</sup> and mechanical strength,<sup>[4]</sup> as well as large specific surface area.<sup>[5]</sup> Together with its high optical transparency, graphene is also promising for application as transparent conductive electrodes.<sup>[6,7]</sup> Nevertheless, the absence of a bandgap in graphene prohibits its use as a semiconductor material, for example, as an active component of a field-effect transistor (FET), and in other optoelectronic devices such as photodetectors, where a suitable bandgap is required.<sup>[8,9]</sup> One of the most promising ways to open up a bandgap in graphene is through structural confinement into nanometer-wide strips, i.e., graphene nanoribbons (GNRs). A GNR can be regarded as a quasi-1D

graphene lattice; therefore, its chemical structure, including the width and edge configuration, strictly determines its electronic and optical properties.<sup>[10–12]</sup> GNRs with armchair and zigzag edges are the most representative, which are called armchair GNRs (AGNRs; **Figure 1a**) and zigzag GNRs (ZGNRs; **Figure 2a**), respectively. The widths of AGNRs and ZGNRs are defined by  $N_a$  and  $N_z$ , respectively (with  $N_a$  and  $N_z$  being the number of carbon atoms in the ribbon width). The electronic structures of AGNRs are sensitive to their width and can be divided into three subfamilies depending on  $N_a = 3n$ ,  $3n+1$ , or  $3n+2$  (where  $n$  is an integer).<sup>[13–15]</sup> All three kinds of AGNRs are expected to be semiconducting materials when they are narrower than 10 nm, and the bandgap in each subfamily scales inversely with the width, while the bandgaps of AGNRs in different subfamilies, but with the same  $n$ , follow the trend of  $3n+2 \ll 3n < 3n+1$ . The charge-carrier mobilities of AGNRs are calculated to decrease with the increasing bandgap and effective mass,<sup>[16]</sup> and thus a fine-tuning of the AGNR width is highly important to achieve an optimal tradeoff between the mobility and bandgap for different applications. In contrast, ZGNRs are predicted to have smaller bandgaps and electronic states localized along the zigzag edges, which are called edge states. It is theoretically predicted that these edge states can be spin


Dr. Z. Chen

State Key Laboratory of Silicon Materials  
School of Materials Science and Engineering  
Zhejiang University  
Hangzhou 310027, China  
E-mail: chenpzp@zju.edu.cn

Prof. A. Narita, Prof. K. Müllen  
Max Planck Institute for Polymer Research  
Ackermannweg 10, D-55128 Mainz, Germany  
E-mail: narita@mpip-mainz.mpg.de; muellen@mpip-mainz.mpg.de

Prof. A. Narita  
Organic and Carbon Nanomaterials Unit  
Okinawa Institute of Science and Technology Graduate University  
Okinawa 904-0495, Japan

Prof. K. Müllen  
Department of Chemistry  
University of Cologne  
Greinstr. 4-6, D-50939 Cologne, Germany

 The ORCID identification number(s) for the author(s) of this article can be found under <https://doi.org/10.1002/adma.202001893>.

© 2020 The Authors. Published by Wiley-VCH GmbH. This is an open access article under the terms of the Creative Commons Attribution License, which permits use, distribution and reproduction in any medium, provided the original work is properly cited.

DOI: 10.1002/adma.202001893

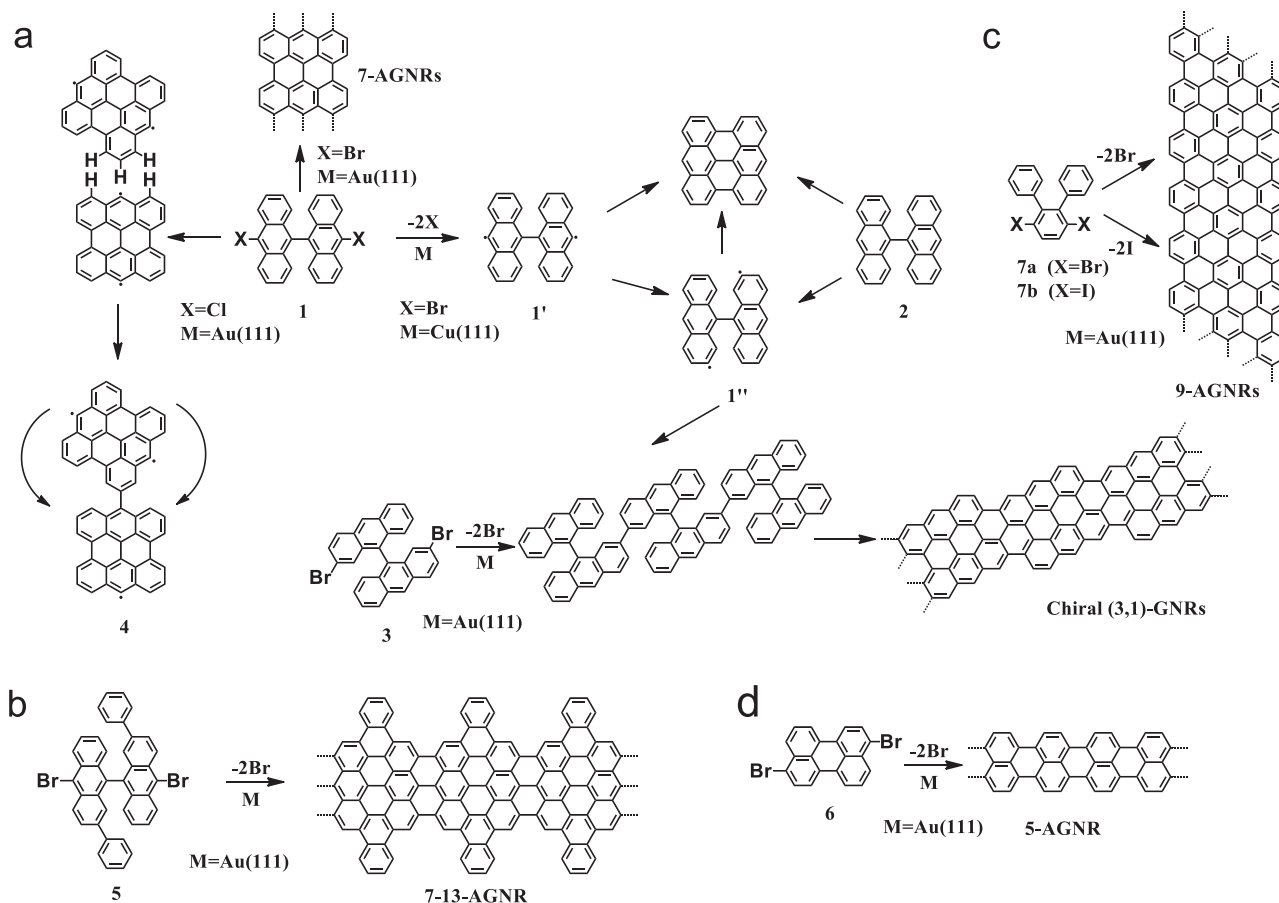


**Figure 1.** a) The choice of substrate and halogen substituent strongly influences the course of the polymerization of 10,10'-dihalo-9,9'-bianthryl (monomer **1**) on surfaces under UHV conditions. b) Synthetic strategy for a new 7-13-AGNR. c) Synthetic route toward 9-AGNRs from monomer **7** containing bromine or iodine, resulting in different length 9-AGNRs. d) Reaction scheme of transforming monomer **6** into a 5-AGNR.

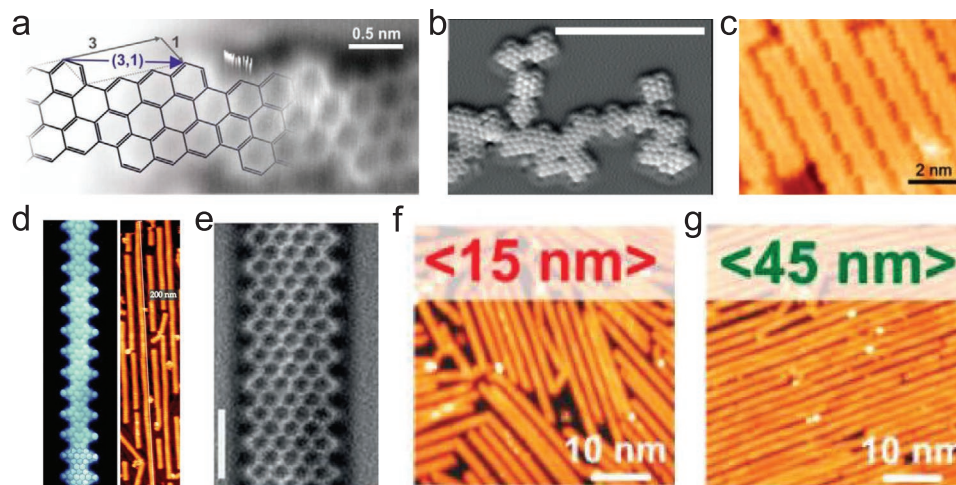


**Figure 2.** a) nc-AFM frequency-shift image of a chiral (3,1)-GNR with a partly overlaid ribbon structure. b) nc-AFM image of structures obtained after annealing DCBA on Au(111). c) High-resolution STM image of parallel chiral (3,1)-GNRs synthesized from monomer **3**. d) High-resolution nc-AFM frequency-shift image (left) and STM image (right) of a single 7-13-AGNR with a length up to 200 nm. e) High-resolution nc-AFM frequency-shift image of a 9-AGNR. f,g) STM images showing different length 9-AGNRs obtained from DBTP (15 nm) and DITP (45 nm). a) Reproduced with permission.<sup>[59]</sup> Copyright 2016, American Chemical Society. b) Reproduced with permission.<sup>[62]</sup> Copyright 2016, Wiley-VCH. c) Reproduced with permission.<sup>[61]</sup> Copyright 2016, American Chemical Society. (https://pubs.acs.org/doi/10.1021/acsnano.6b05269, further permissions related to the material excerpted should be directed to the ACS.) d) Reproduced with permission.<sup>[63]</sup> Copyright 2018, The Royal Society of Chemistry. e) Reproduced with permission.<sup>[64]</sup> Copyright 2017, American Chemical Society. f,g) Reproduced with permission.<sup>[65]</sup> Copyright 2018, American Chemical Society.

polarized, rendering ZGNRs of great potential for spintronic applications.<sup>[17]</sup>

Since their properties are greatly structure dependent, it is essential to synthesize GNRs in an atomically precise fashion without defects to fulfill their targeted function. A number of top-down approaches have been developed for the fabrication of GNRs, which are typically based on the cutting of graphene, for example, through lithographical patterning<sup>[18–21]</sup> and sonochemical treatment in solution.<sup>[22]</sup> Another typical top-down method is unzipping of carbon nanotubes by plasma etching<sup>[23]</sup> or chemical oxidation.<sup>[24]</sup> While not downplaying the value of such practical top-down protocols, they can hardly control the width and especially the edge structure of the GNRs at the atomic level, and only chemically less defined GNRs can thus be obtained, often without accurate control over the properties. Instead, starting from tailor-made organic precursors, it is possible to obtain GNRs with precise atomic control based on bottom-up chemical synthesis. GNRs with different widths and edge structures have thus been synthesized, including armchair, zigzag, chevron-type, and cove structures as well as their combinations.<sup>[10–12,25]</sup>

The bottom-up synthesis of GNRs consists of two main pathways: 1) solution-mediated synthesis based solely on synthetic organic and polymer chemistry techniques and 2) surface-assisted synthesis by on-surface techniques, employing precursor molecules that are adequately designed and furnished through multistep organic synthesis in solution.<sup>[10–12,25,26]</sup> In the solution-mediated synthesis of GNRs, corresponding polyphe-nylene precursors are constructed such that the desired GNRs can be obtained by C–C bond formation between the benzene rings.<sup>[11]</sup> Such polymer precursors are fabricated via different polymerization methods, such as Diels–Alder polymerization,<sup>[27–30]</sup> Yamamoto polymerization,<sup>[31,32]</sup> Suzuki polymerization,<sup>[31]</sup> and living annulative  $\pi$ -extension polymerization.<sup>[33,34]</sup> The resulting polymer precursors are subsequently “planarized” by oxidative cyclodehydrogenation. This solution synthesis can be scaled up to the gram scale<sup>[35]</sup> and allows various edge functionalizations, which are more difficult to achieve through on-surface synthesis.<sup>[36–38]</sup> Notably, introduction of long alkyl chains and other bulky functional groups renders the resulting GNRs dispersible in organic solvents and thus allows for the liquid-phase processing for further characterizations and device fabrication.<sup>[29,34,39,40]</sup> Moreover, the introduction of spin-bearing nitronyl-nitroxide radicals at the edges of a GNR induces magnetic edge states in the GNR, which still remains challenging to achieve using on-surface synthesis.<sup>[41]</sup>

In the surface-assisted synthesis of GNRs, homolytic carbon-halogen cleavage is thermally induced, and the resulting diradicals undergo polymerization to form linear polymers on a metal surface, typically Au(111). Subsequent annealing of the polymers at higher temperatures results in the formation of GNRs through surface-assisted intramolecular cyclodehydrogenation.<sup>[10]</sup> The on-surface synthesis was initially exclusively carried out under ultrahigh vacuum (UHV) conditions with pressures lower than  $\approx 10^{-9}$  mbar, for which in situ high-resolution scanning tunneling microscopy (STM) has unambiguously visualized atomically precise structures of the resulting GNRs. Recent progress made by employing less-demanding high vacuum (HV)<sup>[42]</sup> as well as lower vacuum and even ambient pressure conditions, using an industry-viable chemical vapor

deposition (CVD) setup,<sup>[43–47]</sup> has led to the successful on-surface synthesis of GNRs with the same structures as those synthesized under UHV. Although the length of the GNRs and the defect density might be compromised, the CVD method can substantially scale up GNR production and reduce costs, which are critical requirements for wider application of such bottom-up synthesized GNRs. The films of GNRs synthesized on metal surfaces, which are typically supported on mica substrates, can be transferred to other substrates either by dissolving the metal surface or electrochemically delaminating the GNR films, thus enabling their integration into electronic devices.<sup>[6,48]</sup>

After our previous comprehensive review article in 2015,<sup>[11]</sup> there have been a growing number of reports on the bottom-up synthesis of GNRs as well as their characterization and device applications. In this article, we summarize the latest developments and updates, mainly focusing on the field of on-surface synthesis of GNRs. In view of the dynamics of the field, readers are referred to previous review articles published by us<sup>[11,12,25,26,49–51]</sup> and others<sup>[10,52–56]</sup> for a detailed description of the preceding works. Here, we start with the recent progress in the surface-assisted synthesis of GNRs under UHV and CVD conditions. Then, we address the updates in the applications of on-surface synthesized GNRs, especially directed toward FET devices. We also provide our judgment on the future challenges and perspectives on the bottom-up on-surface synthesis of GNRs.

## 2. Recent Progress in the Surface-Assisted Synthesis of GNRs

### 2.1. On-Surface Synthesis under UHV Conditions

#### 2.1.1. Armchair GNRs

As demonstrated in 2010 for the first time, 10,10'-dibromo-9,9'-bianthryl (**DBBA**) can be thermally polymerized and planarized into  $N = 7$  AGNRs (7-AGNRs) on a Au(111) surface.<sup>[57]</sup> In 2014, Hitosugi and co-workers reported that the polymerization of **DBBA** was strongly substrate dependent.<sup>[58]</sup> When the polymerization of **DBBA** was carried out on Cu(111), a chiral (3,1)-GNR (here, chiral GNRs represent another type of ribbon structure with a combination of armchair and zigzag edges, and the chirality of such a GNR is characterized by the chiral vector  $(n,m)$ ) could be selectively obtained, rather than 7-AGNRs (Figure 1). Fasel and co-workers carried out more precise investigations using noncontact atomic force microscopy (nc-AFM) with CO-functionalized tips under UHV conditions and clearly revealed the atomic structure of the chiral (3,1)-GNRs (Figure 2a).<sup>[59]</sup> Moreover, the identical chiral (3,1)-GNRs were obtained starting from the unsubstituted derivative of **DBBA**, 9,9'-bianthryl (monomer **2**), which highlights the possibility of using halogen-free C–H-activation to obtain atomically precise GNRs (Figure 1a).<sup>[59]</sup> Based on this synthetic concept, Asao and co-workers demonstrated surface-assisted molecular assembly, which connected individual chiral GNRs end to end to form elbow junctions with electronic connections.<sup>[60]</sup> While the chiral (3,1)-GNRs were only synthesized on a Cu(111) substrate using **DBBA**, Peña and co-workers more recently reported substrate-independent

growth of chiral (3,1)-GNRs using 2,2'-dibromo-9,9'-bianthracene (monomer **3**) bearing bromo groups at the desired reaction positions (Figure 2c).<sup>[61]</sup>

Since the electronic structure of AGNRs depends on their width, fine-tuning the electronic bandgap of AGNRs by controlling their width has been one of the most important targets in the field. 7-AGNRs, which have been employed in many previous studies, belong to the AGNR subfamily ( $N = 3n+1$ ) with large bandgaps. Crommie and co-workers reported 13-AGNRs, which belong to the same subfamily as 7-AGNRs but are much wider.<sup>[66]</sup> Scanning tunneling spectroscopy (STS) revealed that the bandgap of 13-AGNRs is 1.4 eV, which is  $\approx 1.0$  eV smaller than the gap previously determined for the narrower 7-AGNRs.<sup>[67,68]</sup> In 2017, we reported a dibromo-*o*-terphenyl (**DBTP**, **7a**) as a suitable molecular precursor for efficient on-surface synthesis of 9-AGNRs (Figure 2e), which belong to the  $N = 3n$  subfamily with medium bandgaps.<sup>[64]</sup> STS measurements disclosed a bandgap of 1.4 eV, similar to that of the wider 13-AGNR.<sup>[69]</sup>

In contrast to the other two AGNR subfamilies, the third subfamily with  $N = 3n+2$  has been predicted to be metallic with zero bandgap at the tight-binding level of theory and semiconducting with very small bandgaps by first-principles calculations.<sup>[14]</sup> On-surface synthesis using 1,4,5,8-tetrabromonaphthalene (**TBN**) as a monomer led to 5-AGNRs, the narrowest possible GNR belonging to the  $N = 3n+2$  subfamily, although the predicted low bandgap could not be revealed.<sup>[70]</sup> On the other hand, Liljeroth and co-workers synthesized 5-AGNRs using another monomer, 3,9 (10)-dibromoperylene (**DBP**, **6**) (Figure 1d), which was previously used by Nakae and co-workers under CVD conditions,<sup>[46]</sup> and elucidated a very small bandgap of  $\approx 100$  meV.<sup>[71]</sup> They also demonstrated that the bandgaps of very short 5-AGNRs were length dependent, with shorter 5-AGNR segments having relatively large bandgaps, which decreased to  $\approx 100$  meV at a length of  $\approx 5$  nm. A length dependence of the bandgap was also found in 7-AGNRs. For the 7-AGNRs longer than 8 nm, the bandgap exhibited a constant value of  $\approx 2.3$  eV, while for those shorter than  $\approx 8$  nm, a decrease in the length could give rise to an increase in the bandgap.<sup>[72]</sup>

The on-surface synthesis of GNRs has thus far mainly employed bromo (Br)-substituted precursors for aryl-aryl coupling based on the homolytic cleavage of C-Br bonds. Investigation of the feasibility of other halogen-substituted precursors for GNR synthesis is highly desirable because it may increase the versatility and selectivity of the synthesis of precursor monomers. In 2016, Swart and co-workers utilized chloride-substituted bianthryl (10,10'-dichloro-9,9'-bianthryl, **DCBA**) for 7-AGNR synthesis on Au(111) (Figures 1a and 2b).<sup>[62]</sup> However, different from the synthesis of 7-AGNRs using **DBBA**, they found that intramolecular cyclodehydrogenation occurred within the **DCBA** molecule, transforming it into a planar bisanthene diradical before dechlorination and polymerization, which was ascribed to an elevated dehalogenation temperature relative to that of **DBBA**. The resulting planar bisanthene diradicals formed highly branched polybisanthene structures, rather than 7-AGNRs, with predominantly fluoranthene-type connections, forming five-membered rings upon further annealing (Figure 2b). Nevertheless, they further found that **DCBA** reacted on Ag(111) to afford both 7-AGNRs and

chiral (3,1)-GNRs because of the more reactive surface, which decreased the dechlorination temperature with respect to that on Au(111).<sup>[73]</sup>

Moreover, based on the iodine-containing monomer diiodo-*o*-terphenyl (**DITP**, **7b**), longer 9-AGNRs (average length of 45 nm) were obtained compared to those synthesized with **DBTP** (average length of 15 nm) (Figures 1c and 2f,g).<sup>[65]</sup> High-resolution X-ray photoelectron spectroscopy (XPS) analyses at different temperatures during the on-surface synthesis revealed the different lengths achieved by the two monomers. This finding can be explained by the lower dehalogenation temperature of **DITP** than that of **DBTP**. A larger difference between the polymerization and cyclodehydrogenation temperatures with reduced "cross-talk" between the two steps can prevent passivation of the radicals at the ends of the growing chains by atomic hydrogen released due to premature cyclodehydrogenation. These results highlight the importance of the halogen function and the metal surface in controlling the on-surface reactions. Moreover, the long 9-AGNRs synthesized by **DITP** produced parallelly ordered arrays on a Au(111) surface with a dense alignment. Aligning GNRs in one direction is essential not only for spectroscopic characterization, such as by angle-resolved ultraviolet photoemission spectroscopy, but also for fabrication of devices in a controlled manner. The most common strategy for the synthesis of aligned GNRs relies on the use of stepped surfaces such as Au(788).<sup>[74]</sup> In 2018, Moreno et al. reported the fabrication of dense arrays of parallelly aligned ultralong GNRs (up to 200 nm) on a Au(111) surface by employing a newly designed precursor, 10,10'-dibromo-2,2'-diphenyl-9,9'-bianthracene (diphenyl-modified **DBBA**, **DP-DBBA**, monomer **5**) (Figures 1b and 2d).<sup>[63]</sup> When the **DP-DBBA** monomer was deposited on the Au(111) surface, the additional phenyl substituents pointed toward the surface, resulting in a weaker molecule-surface interaction and a higher diffusion rate. The direction of the polymerization followed the herringbone reconstruction of the Au(111) surface, inducing parallel alignment of the resulting GNRs. Different from the armchair edge in 7-AGNRs made from **DBBA**, the edge of GNRs synthesized from **DP-DBBA** possesses a periodic arrangement of bays separated by benzo-fused rings formed through the cyclization of the phenyl substituents. The resulting structure can be seen as a series of consecutive pairs of 7- and 13-carbon-atom-wide segments, thus labeled 7-13-AGNR. A small bandgap of 1.0 eV was observed for 7-13-AGNR by STS,<sup>[75]</sup> which is much smaller than that of 7-AGNRs (2.4 eV) and even smaller than that of 13-AGNRs ( $\approx 1.4$  eV).<sup>[69,76]</sup> This result indicates the relevance of the precise edge structure. It is useful to deviate from the pristine armchair edge to obtain additional control over the electronic properties of GNRs.

It should be noted that GNRs and gold surfaces have a strong interaction, and the bandgaps of GNRs obtained via STS measurements on a gold substrate are influenced by the so-called screening effect.<sup>[77,78]</sup> Therefore, the bandgap values measured by STS on a gold surface are generally smaller than the intrinsic electronic bandgaps of the GNRs, which can be theoretically reproduced by the image-charge model proposed by Khariche and Meunier.<sup>[79]</sup> On the other hand, accurate STS measurements of GNRs are also hindered by the concomitant surface states of the underlying gold. Ruffieux and

co-workers recently introduced a Au–Si surface alloying approach to tackle this problem and thus unambiguously determine the electronic bandgaps of AGNRs, although still affected by the screening effect, by in situ intercalation of Si at the AGNR/Au(111) interface.<sup>[77]</sup> As a consequence, the bandgaps of 7- and 9-AGNRs could be more precisely determined to be 2.7 and 1.5 eV, respectively, which were slightly wider than those measured directly on Au(111) (2.4 and 1.4 eV for 7- and 9-AGNRs, respectively). Another concept for controlling the substrate–adsorbate interaction was proposed by Li and co-workers.<sup>[80]</sup> For decoupling from the gold substrate, polymer precursors were grown atop the first layer of 7-AGNRs, which were in direct contact with Au(111). Rather than proceeding to surface-assisted cyclodehydrogenation, an STM tip was used to inject charges at selected molecular sites of the quasi-freestanding polymers to trigger domino-like step-by-step cyclodehydrogenation and form quasi-freestanding 7-AGNRs. It appeared that the bandgap of the second-layer GNR was generally  $\approx 0.1$ – $0.4$  eV greater than that of the first-layer GNR, suggesting a reduced screening effect from the substrate.

### 2.1.2. Zigzag GNRs

Contrary to AGNRs, ZGNRs host electronic states localized along the zigzag edges that can be spin polarized.<sup>[81]</sup> Fasel and co-workers investigated the short zigzag edges at both ends of 7-AGNRs synthesized from DBBA, which were found to possess localized states during the experiments, in agreement with the open-shell biradical character of higher anthenes, namely, of the short 7-AGNRs synthesized and investigated by Kubo and co-workers through solution chemistry.<sup>[81]</sup> The 7-AGNRs with different lengths (i.e., different distances between their two terminating zigzag edges) were transferred onto insulating sodium chloride islands using an STM tip. Thus, the nanoribbons could be decoupled from the Au surface, allowing for precise analysis of the zigzag termini via STM. A pair of occupied/unoccupied edge states was revealed with a large energy splitting of 1.9 eV, which could be ascribed to electron–electron interactions in the localized states. The energy splitting was independent of the distance between the two zigzag edges, namely, the length of the 7-AGNR, down to 3 nm.

The synthesis of ZGNRs was one of the biggest challenges faced by the research community. This was apparently because the zigzag edge could not be obtained through conventional C–C bond formation between benzene rings, which would only result in an armchair edge. To this end, preinstallation of zigzag edge segments in the precursor structure was considered, along with a use of a methyl group, which was expected to form a C–C bond with a neighboring benzene ring (Figure 3a, b,i,j).<sup>[82]</sup> Based on this basic concept, U-shaped monomer **8a** functionalized with two bromo groups as well as two methyl groups was designed (labeled in red in Figure 3a). Upon thermal treatment on a Au(111) surface, precursor **8a** could be successfully polymerized and then planarized, accomplishing the desired oxidative cyclization of the methyl groups to produce extended zigzag edges (the formed new bonds are labeled in blue in Figure 3a), which led to  $N = 6$  ZGNRs

(6-ZGNRs) with pure zigzag edges. Transfer of 6-ZGNRs onto NaCl islands by tip manipulation allowed the demonstration of three resonance peaks near the Fermi level with energy splittings of 1.5 and 1.9 eV between the two occupied states and the unoccupied one, as determined by STS measurements close to the zigzag edges. Precursor **8b** was also synthesized with an additional phenyl group on the zigzag edge, which was intended to give kinetic protection to the labile zigzag edge and to decouple the ZGNR from the metal surface.<sup>[82]</sup> Interestingly, nc-AFM imaging of the resulting GNRs obtained from **8b** on Au(111) revealed that the additional phenyl rings unexpectedly reacted with the zigzag edges to form fluoranthenic subunits with an incorporated five-membered ring at the given graphitization temperature. The additional fluoranthene units efficiently decreased the interactions between the ZGNRs and the surface, despite the planarized structure, which allowed simple visualization of the edge states directly on the metal. On the other hand, it must be noted that the cyclization of the phenyl groups, either to the right or left side of the zigzag edge, was random, precluding the formation of a fully periodic structure.

### 2.1.3. Chevron-Type GNRs

In addition to 7-AGNRs, the so-called chevron-type GNRs are another extensively studied example of GNRs on surfaces (Figure 4a).<sup>[57]</sup> Chevron-type GNRs were synthesized on a Au(111) surface by thermal polymerization of the monomer 6,11-dibromo-1,2,3,4-tetraphenyltriphenylene (DBTT, monomer **12**), followed by planarization. Recently, in collaboration with Fasel's group, we could unequivocally identify the different reaction stages in the synthesis of chevron-type GNRs based on reflectance difference and high-resolution electron energy loss spectroscopies.<sup>[87]</sup> Moreover, it was confirmed that the primary excitations in chevron-type GNRs and their precursor polymers were of an excitonic nature with electron–hole binding energies of  $\approx 1.6$  and 2.0 eV, respectively. The synthesis of chevron-type GNRs was also found to be substrate dependent. Sinitskii and co-workers synthesized chevron-type GNRs on a Cu(111) surface using the same monomer DBTT.<sup>[88]</sup> They found that the GNRs aligned epitaxially along the  $\langle 112 \rangle$  crystallographic direction, which was not observed with these GNRs grown on Au(111) (Figure 4e). The pronounced epitaxial effect seen for the Cu(111) surface is due to the energetic preference of carbon atoms to sit on top of Cu atoms. The directional control of atomically precise GNRs by choosing different crystalline substrates may eventually facilitate the fabrication of GNR electronic devices without the need to rely on the special terrace structure on the Au(788) surface for alignment of GNRs.<sup>[74]</sup>

On the other hand, the ease of structural derivatization of DBTT through Diels–Alder cycloaddition of the corresponding starting material based on a cyclopentadienone and different (di)arylacetylenes in the final step of the preparation prompted us as well as many other researchers to synthesize various GNRs based on the chevron-type GNR structure. Heteroatom-doped chevron-type GNRs will be discussed in the next subsection. Sinitskii and co-workers reported phenyl-functionalized chevron-type GNRs by attaching additional phenyl groups

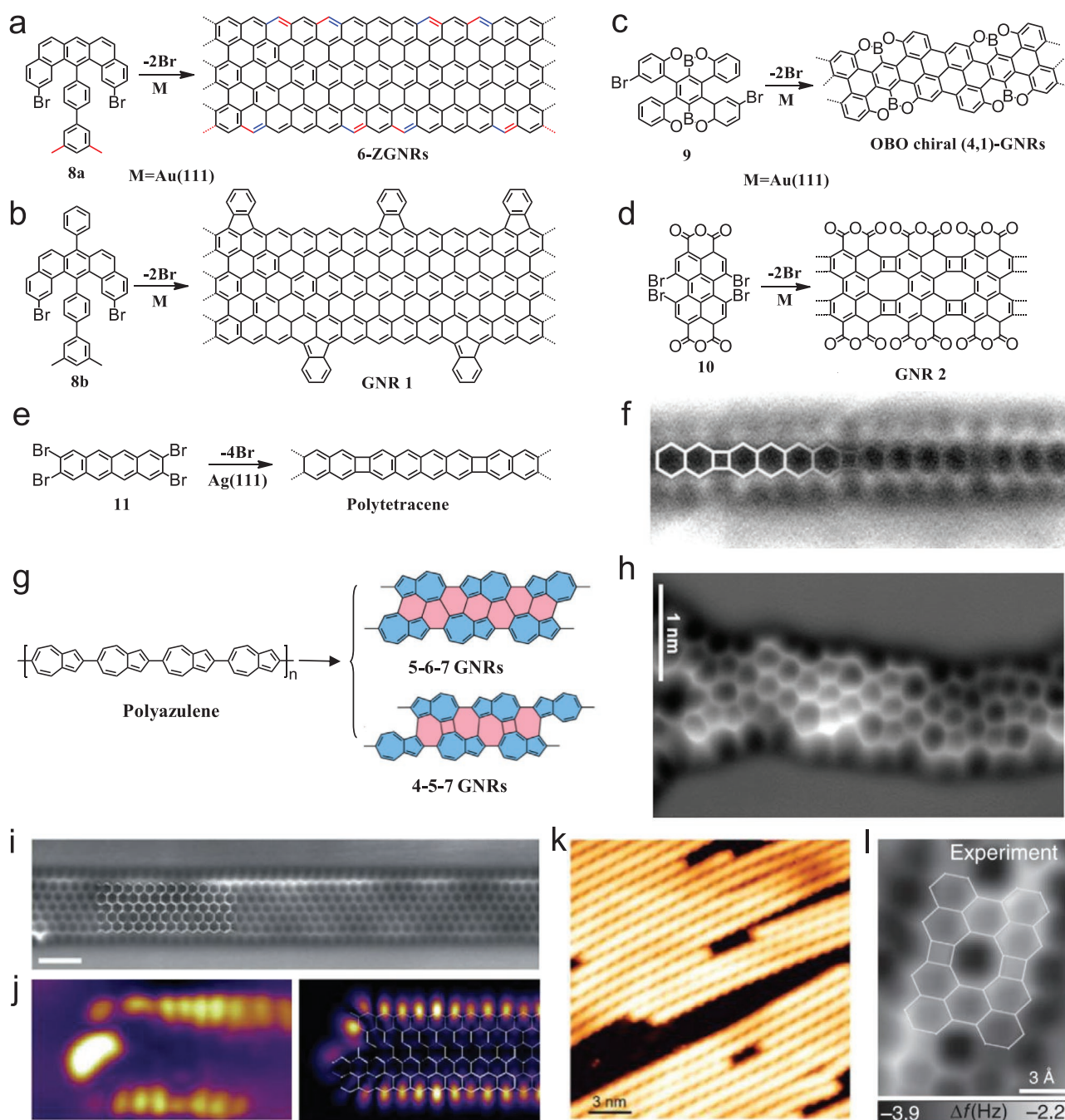


**Figure 3.** a,b) Synthetic route toward a full zigzag GNR from umbrella-shaped monomer **8a** and modified **GNR 1** from monomer **8b**. The methyl groups are labeled in red, and the new bonds formed by oxidative cyclization of the methyl groups with the neighboring aromatic rings are labeled in blue. c) Synthetic route for the chiral (4,1)-GNR. d) Synthetic strategy for graphene-like nanoribbons. e) Reaction scheme for the formation of polytetracene-based nanoribbons. f) nc-AFM image of the polytetracene-based nanoribbons. g) Lateral fusion of two polyazulene chains into GNRs rich with nonhexagonal rings, including 5-6-7- and 4-5-7-membered rings. h) Constant-height AFM image of a typical 5-6-7 GNR. i) Constant height nc-AFM frequency shift image of a ZGNR taken with a CO-functionalized tip. j) Differential conductance maps of filled edge states taken at a sample bias of 0.3 V (left), and DFT-based local density of states (DOS) at a tip-sample distance of 4 Å, showing the spatial distribution of filled edge states (right). All scale bars are 1 nm. k) STM overview of chiral (4,1)-GNRs. l) Constant-height nc-AFM frequency shift image of a graphene-like nanoribbon resolving four- and eight-membered rings taken with a partly overlaid ribbon structure. f) Reproduced with permission.<sup>[83]</sup> Copyright 2019, Wiley-VCH. g,h) Reproduced with permission.<sup>[84]</sup> Copyright 2019, American Chemical Society. i,j) Reproduced with permission.<sup>[82]</sup> Copyright 2016, Springer Nature. k) Reproduced with permission.<sup>[85]</sup> Copyright 2018, American Chemical Society. l) Reproduced under the terms of the CC-BY Creative Commons Attribution 4.0 International license (<http://creativecommons.org/licenses/by/4.0>).<sup>[86]</sup> Copyright 2017, The Authors, published by Springer Nature.

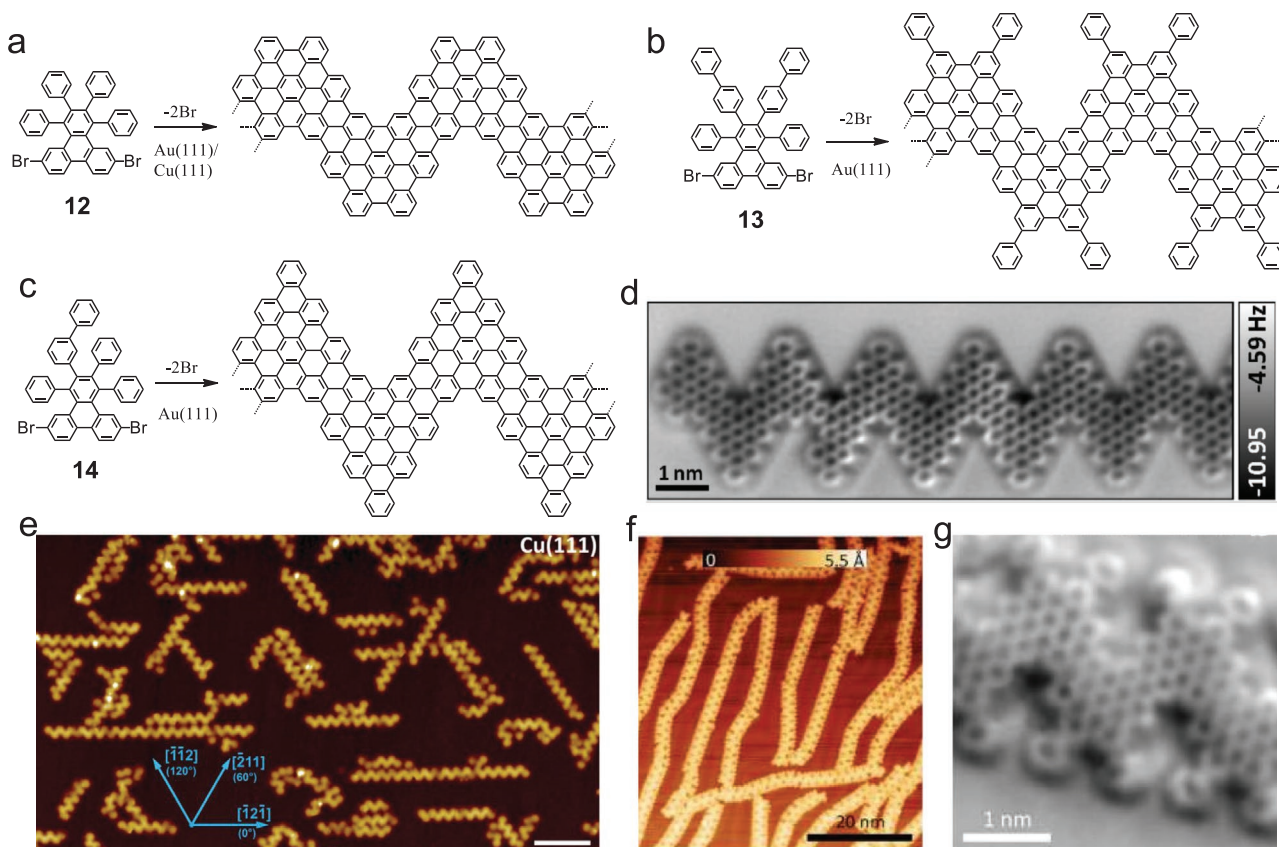


**Figure 4.** a–c) On-surface synthesis of: a) chevron-type GNRs, b) phenyl-modified chevron-type GNRs, and c) laterally extended chevron-type GNRs using monomers **12**, **13**, and **14**, respectively. d) nc-AFM image of laterally extended chevron-type GNRs. e) STM image of chevron-type GNRs on Cu(111) with visible epitaxial arrangement; scale bar: 10 nm. f, g) STM and nc-AFM images of phenyl-modified chevron-type GNRs on Au(111). d) Reproduced with permission.<sup>[89]</sup> Copyright 2019, Wiley-VCH. e) Reproduced with permission.<sup>[88]</sup> Copyright 2017, The Royal Society of Chemistry. f, g) Reproduced with permission.<sup>[90]</sup> Copyright 2018, American Chemical Society.

to the monomer **DBTT** (Figure 4b,f,g).<sup>[90]</sup> The bandgap of the phenyl-modified GNRs on Au(111) revealed by STS was  $\approx 2.50$  eV, which was comparable to that of the parent chevron-type GNRs. However, the phenyl functionalization resulted in GNRs with band edges downshifted by  $\approx 0.1$  eV. Moreover, the additional phenyl substituents enhanced the  $\pi$ - $\pi$  interactions and facilitated the side-by-side assembly of the GNRs. Upon annealing, the phenyl units of two adjacent ribbons could be fused together by intermolecular cyclodehydrogenation, resulting in atomically precise graphene nanopores. In 2018, Sinitskii and co-workers further synthesized a laterally extended chevron-type GNR that contained an additional benzene ring in the elbow positions using a new monomer **14** (Figure 4c,d).<sup>[89,91]</sup> The lateral extension of the chevron-type GNR resulted in a small reduction in the bandgap from 1.61 to 1.38 eV according to density functional theory (DFT) calculations.<sup>[92]</sup>

#### 2.1.4. GNRs with Other Structures

In addition to the abovementioned armchair, zigzag, and chevron-type GNRs, the development of GNRs with other edge structures is also noteworthy. In 2015, a chrysene-type monomer was reported for the synthesis of an unprecedented cove-edge

GNR. Theoretical calculations predicted that such cove-edge GNRs possess a relatively low bandgap of 1.70 eV.<sup>[93]</sup> Chiral GNRs are another important type of ribbon structure with localized edge states that depend on the chirality.<sup>[94]</sup> However, only the synthesis of chiral (3,1)-GNRs has been achieved.<sup>[59,61]</sup> In collaboration with Fasel's group, we recently synthesized an oxygen–boron–oxygen-doped chiral (4,1)-GNR using a specially designed precursor **9** (Figure 3c,k).<sup>[85]</sup> A highly regular alignment of the GNRs on a Au(111) surface was found. Such lateral self-assembly arises from strong inter-ribbon  $O \cdots H$  interactions. Such self-assembly behavior has also been demonstrated for nitrogen-doped GNRs and can be a useful tool for controlling the assembly of GNRs on surfaces.<sup>[95]</sup>

To date, most of the reported GNRs are composed of graphene lattices with hexagonal carbon rings. Embedding nonhexagonal rings into  $sp^2$ -hybridized graphene lattices can be a promising strategy to modify the electronic structures. In 2017, Zhong and co-workers reported on-surface synthesis of graphene-like nanoribbons with periodically embedded four- and eight-membered rings, which were formed between adjacent perylene backbones in a planar configuration (Figure 3d,j).<sup>[86]</sup> STS revealed an electronic bandgap of 1.38 eV for this new graphene-like nanoribbon, and the lowest unoccupied and highest occupied states were mainly distributed

around the four- and eight-membered rings, respectively. Recently, a unique tetracene-based nanoribbon was described, which incorporated four-membered rings as linkers between the acene segments through a formal [2+2] cycloaddition reaction of tetrabromotetracene monomer **11** (Figure 3e–f).<sup>[83]</sup> The formation of four-membered rings between tetracenes has been unambiguously proven by nc-AFM imaging with CO-functionalized tips. STS measurements revealed an electronic bandgap of  $\approx 1.6$  eV for the nanoribbons with tetracene building blocks, in good agreement with the DFT-predicted value of 1.64 eV. More recently, Gottfried and co-workers demonstrated two new GNRs with 5-6-7- and 4-5-7-membered rings by lateral dehydrogenative fusion of polyazulene chains on Au (111) surface (Figure 3g,h). These two different structures are determined by the relative positions of the fused polyazulene chains.<sup>[84]</sup>

### 2.1.5. Doping of GNRs

The size of the bandgaps of GNRs can be engineered by varying their width and edge structures as introduced above, but the alignment of their band structure with respect to the Fermi level of a metal electrode is equally important for their integration into electronic devices. In 2013, Tegeder and co-workers reported that the electronic properties of GNRs can be controlled by nitrogen (N) doping.<sup>[96]</sup> They successfully synthesized N-doped chevron-type GNRs by selective incorporation of either one or two N atoms into the parent **DBTT** monomer. Continuous downshifting of the binding energy of  $\approx 0.1$  eV per N atom was observed, suggesting that heteroatom doping could be a powerful way to engineer the electronic structures of GNRs. Indeed, a large band offset of up to 0.5 eV was also observed for N-doped chevron-type GNRs with four N atoms per monomer unit.<sup>[95]</sup> Nevertheless, the size of the bandgap of the N-doped chevron-type GNRs was nearly unchanged compared with that of the pristine GNRs.<sup>[95,96]</sup> In addition to N doping of chevron-type GNRs, sulfur-substituted oligophenylene monomer **15** was recently proposed for the synthesis of S-doped chevron-type GNRs (Figure 5a,h).<sup>[97]</sup> Different from the N-substituted monomer, intramolecular cyclodehydrogenation of the S-substituted monomer can occur at different sites, resulting in a subfamily of distinct cyclodehydrogenated constitutional isomers. Because of the different S positions and cyclization sites, the final GNRs could possess 17 possible S-doped segments with distinct bandgaps. Therefore, STS measurements at different sites of one ribbon revealed bandgaps ranging from 1.28 to 1.87 eV. Moreover, the C–S bonds in the S-doped GNRs were not stable at elevated annealing temperatures ( $>680$  K).<sup>[98]</sup> In 2018, Fischer and co-workers designed a series of different monomers **16** for the synthesis of chevron-type GNRs with trigonal planar N-, O-, and S-dopant atoms incorporated along the convex protrusions (Figure 5b,i).<sup>[99]</sup> The varying electronegativity of the N-, O-, and S-dopant atoms induced different degrees of charge transfer between the dopant atoms and the GNR backbone. The O and S dopants acted as acceptors withdrawing 0.17 and 0.12 electrons per O- and S-dopant atom from the GNR backbone, respectively, while the N dopants served as donors contributing 0.11 electrons per N atom to the GNR. STS measurements revealed bandgaps for

N-, O-, and S-doped GNRs of 2.2, 2.3, and 2.2 eV, respectively, which were  $\approx 0.2$ – $0.3$  eV smaller than those of the unsubstituted chevron-type GNRs ( $\approx 2.5$  eV). This could be explained by the overlapping of the heteroatom lone pairs with the extended  $\pi$ -system of the GNR backbone.

In addition to doped chevron-type GNRs, heteroatom-doped AGNRs have also been synthesized. In 2015, Kawai et al. and Fischer and co-workers independently reported boron (B)-doped 7-AGNRs (B-7-AGNRs) based on the polymerization and subsequent planarization of B-doped precursor **18** (Figure 5d,f,g).<sup>[100,103]</sup> The atomic structure of the B-doped GNRs, including the B–C bonds, was verified via nc-AFM imaging. The presence of boron atoms induced stronger coupling between the B-7-AGNRs and the Au(111) substrate, while the STS measurement revealed a bandgap of 2.4 eV for B-7-AGNRs, which was comparable to that of pristine 7-AGNRs on Au(111).<sup>[67]</sup> In addition to B-7-AGNRs, wider boron-doped GNRs, such as B-14/21-AGNRs, were formed via a cross-dehydrogenative coupling reaction of two/three B-7-AGNRs, respectively, by annealing the B-7-AGNRs at a higher temperature of 510 °C. Furthermore, the chemical reactivity of the doped GNRs was probed via the absorption of nitric oxide, which demonstrated the Lewis acid character of B-7-AGNRs at the boron sites.<sup>[100]</sup> Recently, Fischer and co-workers investigated the electronic structures of B-7-AGNRs with different concentrations of boron dopants by combining B-doped monomer **18** with monomer **1** for pristine 7-AGNRs at different ratios.<sup>[104]</sup> They found that boron dopants in 7-AGNRs induced the formation of two new in-gap dopant states that varied continuously as the boron dopant concentration increased. Moreover, a strong hybridization between the B atoms and the underlying Au(111) substrate was found.<sup>[105]</sup> In 2018, Kawai et al. achieved the synthesis of B- and N-codoped GNRs (BN-GNRs) using monomer **19** (Figure 5e,k,l).<sup>[102]</sup> Although monomer **19** was functionalized with I and Cl with different reactivities, both head-to-tail (C–I to C–Cl) and head-to-head (C–I to C–I followed by C–Cl to C–Cl) couplings were observed, leading to a series of BN-GNRs with different orientations of the unsymmetrical monomer units. nc-AFM with a CO-functionalized tip could facilely elucidate the location and arrangement of the B and N elements in the GNRs due to their differences in van der Waals radii and the relative onset of repulsive interactions. Very recently, Feng and co-workers synthesized nitrogen–boron–nitrogen (NBN)-doped ZGNRs with NBN unit preinstalled at the zigzag edges.<sup>[106]</sup> Due to the NBN edge doping, the GNRs featured stable zigzag edges compared to the highly unstable pristine ZGNRs. In 2016, Fischer and co-workers reported the fabrication of sulfur-doped 13-AGNRs (S-13-AGNRs) by using monomer **17**, which had the scaffold of monomer **1** substituted with two thiophenyl-phenyl units.<sup>[101]</sup> The resulting S-13-AGNRs had one of the lone pairs of each sulfur atom in full conjugation with the aromatic  $\pi$ -system of the underlying 13-AGNR. The electronic structure of S-13-AGNRs revealed enhanced energy separation between the band edges of the conduction band (CB) and CB+1 as well as the valence band (VB) and VB-1, while the energy alignments remained essentially unchanged compared with those of the undoped 13-AGNRs. In 2017, Yamada and co-workers attempted to synthesize edge fluorinated 7-AGNRs using 10,10'-dibromo-2',3',6',7'-tetrafluoro-9,9':10',9'-teranthracene as a precursor



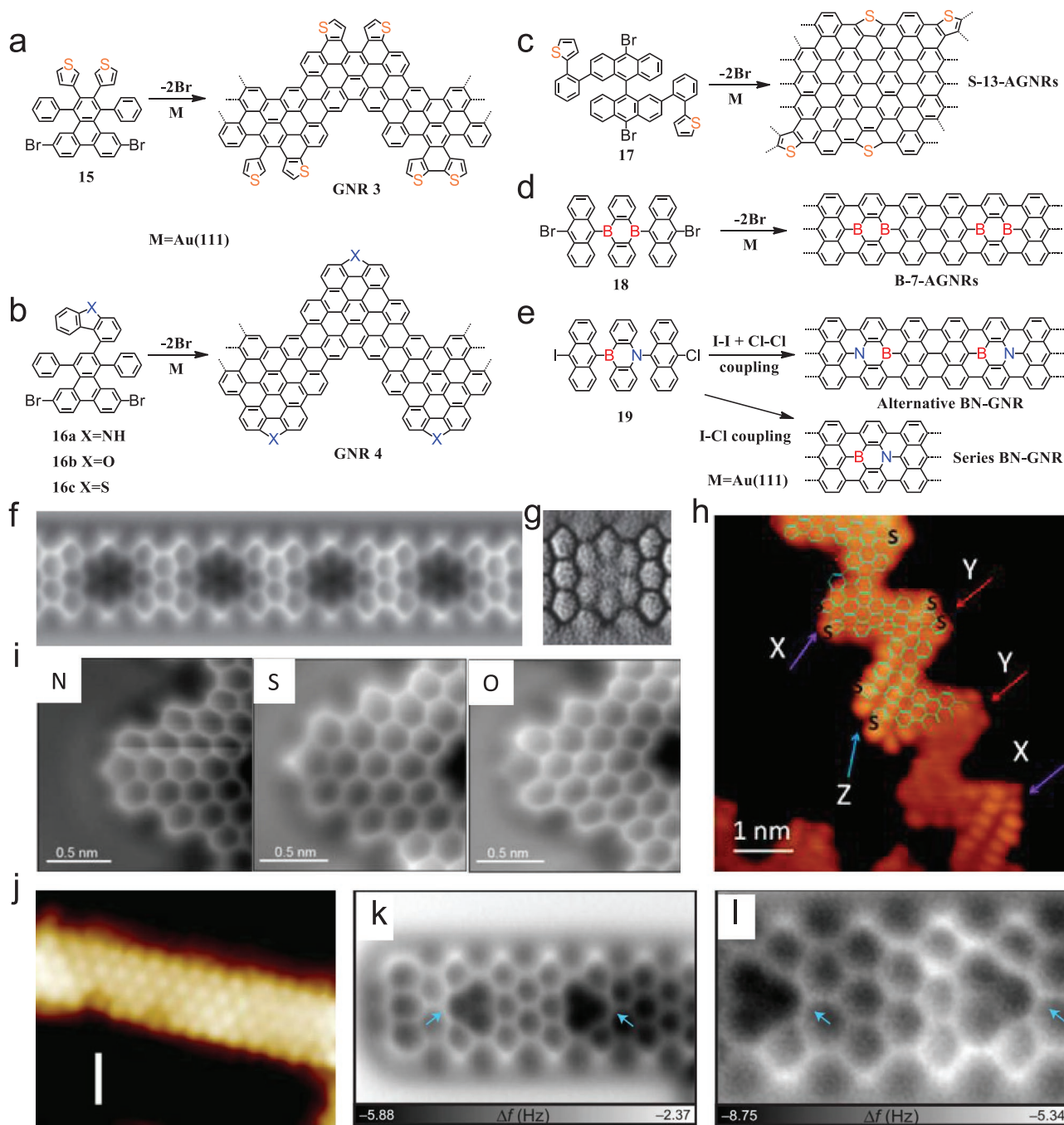


**Figure 5.** a–e) Synthetic routes toward: a) S-GNRs composed of various segments, b) N-, S-, and O-doped GNRs, c) S-13-AGNRs, d) B-7-AGNRs, and e) BN-GNRs. f) nc-AFM frequency shift image of B-7-AGNRs. g) Corresponding Laplace filtered image for a better view of the bonds in B-7-AGNRs. h) High-resolution STM image of S-GNRs with a partly overlaid structural model. i) nc-AFM frequency-shift image of N-, S-, and O-doped GNRs. j) STM image of a S-13-AGNR. k) AFM images of an alternative BN-GNR. l) AFM images of a series BN-GNR. f, g) Reproduced under the terms of the CC-BY Creative Commons Attribution 4.0 International license (<http://creativecommons.org/licenses/by/4.0/>).<sup>[100]</sup> Copyright 2015, Springer Nature. h) Reproduced with permission.<sup>[97]</sup> Copyright 2017, Springer Nature. i) Reproduced with permission.<sup>[99]</sup> Copyright 2017, American Chemical Society. j) Reproduced with permission.<sup>[101]</sup> Copyright 2016, American Chemical Society. k, l) Reproduced with permission.<sup>[102]</sup> Copyright 2018, The Authors, published by American Association for the Advancement of Science (AAAS). Reprinted/adapted from ref. [102]. © The Authors, some rights reserved; exclusive licensee American Association for the Advancement of Science. Distributed under a Creative Commons Attribution NonCommercial License 4.0 (CC BY-NC) <http://creativecommons.org/licenses/by-nc/4.0/>.

molecule.<sup>[107]</sup> However, annealing of the GNRs at 400 °C led to carbon–fluorine bond cleavage. On the other hand, Pascual and co-workers tried to obtain GNRs functionalized with cyano groups at the edge, which induced a downshift of the VB and CB+1 by  $\approx 0.3$  eV per CN added.<sup>[108]</sup> Some of the cyano groups

were cleaved during the cyclodehydrogenation step by  $\sigma$ -bond cleavage, and a fraction of the cyano groups was cyclized and incorporated into the edge of the GNRs as pyridine rings.

Beyond the covalent doping of GNRs by heteroatom substitution, Grüneis and co-workers reported electron doping of GNRs

using physically adsorbed lithium atoms as electron donors.<sup>[109]</sup> One to three monolayers of lithium were in situ deposited on aligned 7-AGNRs grown on a Au(788) surface. Electron transfer from lithium to GNRs resulted in a high doping level of  $\approx 1.7$  electrons  $\text{nm}^{-1}$  or 0.05 electrons per carbon atom. Under such conditions, the 7-AGNRs were found to be transformed from a wide-gap semiconductor into a metal, where the effective mass of electrons in the conduction band increased to a value equal to that of the free electron mass with a much enhanced density of states at the Fermi level.

### 2.1.6. GNR Heterostructures

Fusing two different types of GNR segments together leads to atomically sharp heterojunctions.<sup>[76,95]</sup> Due to the different electronic structures of the two GNR segments, the junction within a single GNR has unique electronic properties. In 2014, the first GNR heterojunction was demonstrated by fusing a pristine chevron-type GNR and its N-doped counterpart, leading to an atomically sharp p–n junction. The electric field within this GNR junction was as high as  $2 \times 10^8$  V  $\text{m}^{-1}$ , at least two orders of magnitude higher than that in traditional semiconductor p–n junctions.<sup>[95]</sup> In the same year, Louie's group successfully fabricated width varying 7-13-GNR heterojunctions, demonstrating a shrunken bandgap in the 13-AGNR segment.<sup>[76]</sup> In 2017, Swart and co-workers synthesized another 5-7-GNR heterojunction.<sup>[110]</sup> The precursors **DBBA** and **DBP** were used to grow semiconducting 7-AGNRs and metallic 5-AGNRs, respectively. Co-deposition of both precursors on Au(111) resulted in 5-7-GNR heterojunctions, which could be characterized as metal–semiconductor junctions. Beyond the single-junction structures, 5/7/5-GNR heterostructures with two junctions were also formed. The 5/7/5-GNR could function as a tunnel barrier, where the semiconducting 7-AGNR “channel” was sandwiched between metallic 5-AGNR “leads”, realizing a complete electronic device within a single GNR. In 2018, Sinitiskii and co-workers reported a GNR heterojunction composed of chevron-type segments and laterally extended chevron-type segments with an additional benzene ring (**Figure 6c,d**).<sup>[91]</sup> The widening of the chevron GNR resulted in a reduction in the bandgap from 1.61 to 1.38 eV according to DFT calculations.<sup>[92]</sup> The heterojunction obtained by combining the chevron-type GNR and the laterally extended GNR demonstrated the possibility of engineering complex GNR-based nanostructures.

In addition to combining two or more different molecular precursors for the synthesis of GNR heterojunctions, Louie's group reported a post growth manipulation method for the fabrication of atomically precise GNR heterojunctions from a single precursor.<sup>[111]</sup> Their strategy relied on a chevron-type GNR with incorporated fluorenone moieties, where the carbonyl group could be removed by thermal annealing or by an electric field induced with an STM tip (**Figure 6a,b**). The fluorenone-incorporating GNRs were found to have lower CB and VB edges as well as an overall reduction in the bandgap of 0.20 eV compared with the pristine chevron-type GNRs (**Figure 4a**). Therefore, the atomically precise interfaces between carbonyl-decorated and carbonyl-free GNR segments furnished a heterojunction. Modification of the GNR electronic properties by post-treatment

could open an additional route for integration and control of GNR heterojunctions for more complex molecular devices. Recently, these groups further designed a molecular building block bearing a 9-methyl-9H-carbazole substituent (monomer **20**) for GNR synthesis.<sup>[112,114]</sup> Remarkably, the carbazole substituent in the GNRs could undergo a secondary thermally induced transformation, which led to either a fused phenanthridine (characterized by a six-membered ring) or a fused carbazole (characterized by a five-membered ring) unit incorporated into the GNRs, resulting in a heterojunction with different segment lengths (**Figure 6e,f**). Owing to their different electron affinities, the carbazole and phenanthridine configurations exhibited electron-donating and electron-withdrawing behavior, respectively, inducing upward and downward orbital energy shifts. The magnitude of the energy offsets of the heterojunction was dependent on the length of the carbazole/phenanthridine segments, with longer segments leading to larger energy offsets. On the other hand, S-doped chevron-type GNRs synthesized from single monomer **15**, as shown in **Figure 5a,h**, were actually heterostructures with segments of isomeric and/or partially fused structures along one ribbon.<sup>[97]</sup> C–S bond cleavage by postannealing can further lead to more complicated heterostructures.<sup>[98]</sup> In addition to heterojunctions with two different GNR segments, Pascual and co-workers and Yu and co-workers independently described that bonding of a single porphyrin molecule with magnetic ions (such as  $\text{Fe}^{2+}$  ions) to the end of a GNR could afford a new kind of heterojunction (**Figure 6g**).<sup>[113,115]</sup> This covalently connected heterojunction extended the electronic conjugation of the ribbon into the connected porphyrin. The spin state was preserved, while the magnetic anisotropy was modified depending on the contact configuration of the heterojunction.

### 2.1.7. Topological Quantum Phases in GNRs

After successful synthesis of zigzag GNRs utilizing the oxidative cyclization of methyl groups to establish zigzag edges, we considered the use of methyl groups to synthesize other novel GNRs with zigzag edges. The dianthryl-dimethyltetracene-based monomer **21** was thus designed, which was expected to provide **GNR 5** with the structure of a 7-AGNR that is extended with zigzag edges.<sup>[116]</sup> In collaboration with Gröning et al., we successfully demonstrated the on-surface synthesis of **GNR 5** starting from monomer **21**, which could be unambiguously revealed by nc-AFM (**Figure 7a,b**). Interestingly, **GNR 5** exhibited a significantly lower bandgap of  $\approx 0.7$  eV, based on STS analysis, in comparison to the  $\approx 2.4$  eV bandgap of the pristine 7-AGNR. Furthermore, the extension of the 7-AGNR with zigzag edges on both sides using dianthryl-tetramethylpentacene-based monomer **22** was considered. The on-surface synthesis using monomer **22** proceeded smoothly to yield **GNR 6**, which was based on the 7-AGNR but was fully “extended” with zigzag edges. Notably, theoretical studies by Gröning based on tight-binding calculations revealed that **GNR 6** was topologically nontrivial, having zero-energy topological states at the ends of the GNR, while **GNR 5** was topologically trivial. The topological end states of **GNR 6** were predicted to be hybridized with another kind of end state known for the zigzag edges at the ends of 7-AGNRs. Therefore, heterojunctions of **GNR 6** and pristine 7-AGNRs were prepared (7-AGNR/**GNR 6**; **Figure 7c,d**)

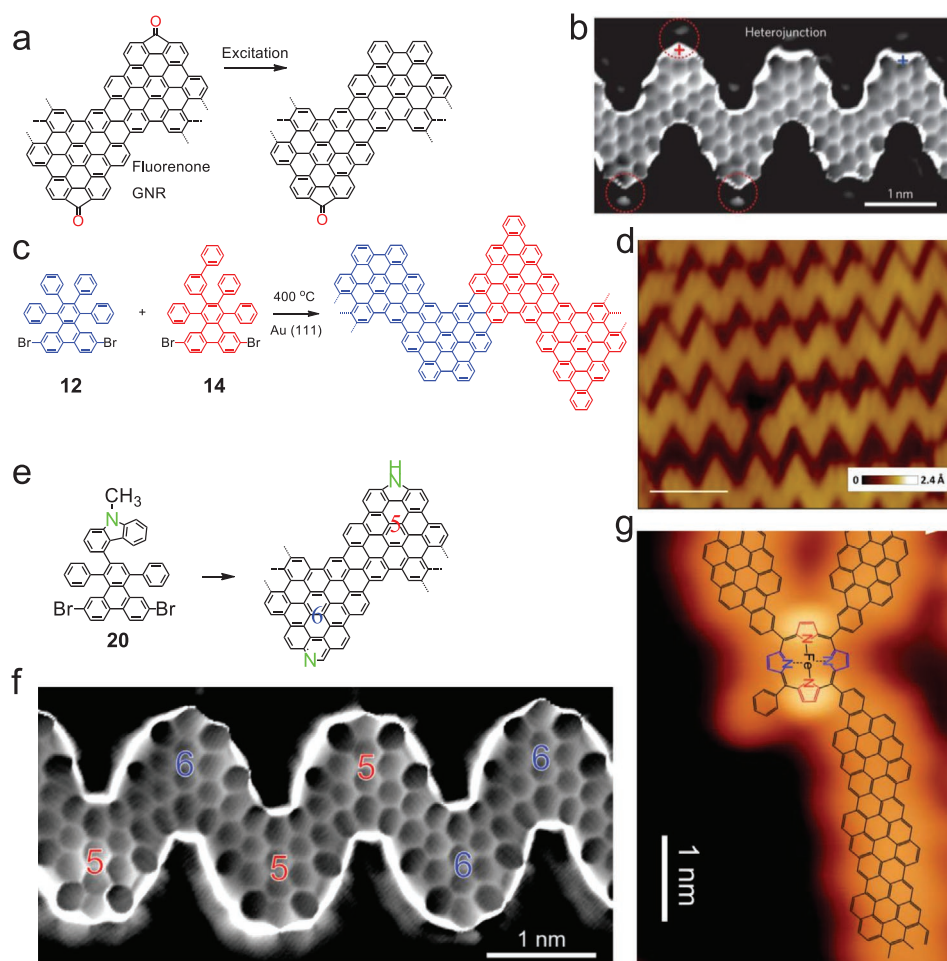


**Figure 6.** a) Schematic representation of the fabrication of a GNR heterojunction from a fluorenone GNR by post-treatment. b) Bond-resolved STM image of a fluorenone/unfunctionalized chevron heterojunction. c) Reaction scheme for the GNR heterojunction combining chevron-type GNRs and laterally extended chevron-type GNRs. d) High-resolution STM images of coincidentally aligned heterostructural GNRs. e,f) Bottom-up fabrication of carbazole (5)/phenanthridine (6) edge-functionalized GNR heterostructures and their typical bond-resolved STM image. g) Constant current STM image of a porphyrin moiety connected to three GNRs. The corresponding structure is superimposed. b) Reproduced with permission.<sup>[111]</sup> Copyright 2017, Springer Nature. d) Reproduced with permission.<sup>[91]</sup> Copyright 2018, Elsevier Ltd. f) Reproduced with permission.<sup>[112]</sup> Copyright 2019, American Chemical Society. g) Reproduced with permission.<sup>[113]</sup> Copyright 2018, The Authors, published by American Association for the Advancement of Science (AAAS). Reprinted/adapted from ref. [113]. © The Authors, some rights reserved; exclusive licensee American Association for the Advancement of Science. Distributed under a Creative Commons Attribution NonCommercial License 4.0 (CC BY-NC) <http://creativecommons.org/licenses/by-nc/4.0/>.

by combining the monomer DBBA and **22** toward an on-surface synthesis. In such heterojunctions, the topological end states of GNR **6** could be unambiguously demonstrated at the interfaces with 7-AGNRs by  $dI/dV$  mapping, in very good agreement with the local density of states obtained by tight-binding calculations (Figure 7e,f). At the same time, Louie's group achieved another topologically nontrivial GNR that had a periodic heterostructure of 7- and 9-AGNRs, starting from monomer **23** (Figure 7g,h).<sup>[117]</sup> The interface between the 7-AGNR and 9-AGNR segments, connected with zigzag edges, constituted an 8-AGNR with zero bandgap at the tight-binding level of theory and possessed localized interface states of a topological nature. Notably, coupling between adjacent 7/9-AGNR topological interface states was found to directly define the band structure of these GNR heterojunctions. These results suggest the great potential of bottom-up-synthesized GNRs as a new platform for developing topological quantum materials.

### 2.1.8. Fusion of GNRs

Branching of GNRs, due to coupling of an end of a GNR to the edge of another one, has been frequently observed during on-surface syntheses,<sup>[57,118,119]</sup> but the precise structure at such junction points has rarely been elucidated. Diemel et al. resolved the atomic structures of the branching sites of 7-AGNRs using nc-AFM (Figure 8a–c).<sup>[120]</sup> The connection of the terminal zigzag edges with the lateral armchair edges resulted in defect structures consisting of both five- and seven-membered rings. On the other hand, the 7-AGNRs grown in close proximity to each other on a Au(111) surface could undergo cross-dehydrogenative coupling along their long axis (coaxial fusion of armchair edges) to give a fully conjugated 14-AGNR or an even wider 21-AGNR by forming new six-membered rings.<sup>[77,118,120]</sup> Lateral fusion has also been found in boron-doped B-7-AGNRs, resulting in wider B-14-AGNRs and B-21-AGNRs (Figure 8d).<sup>[100]</sup> Moreover,

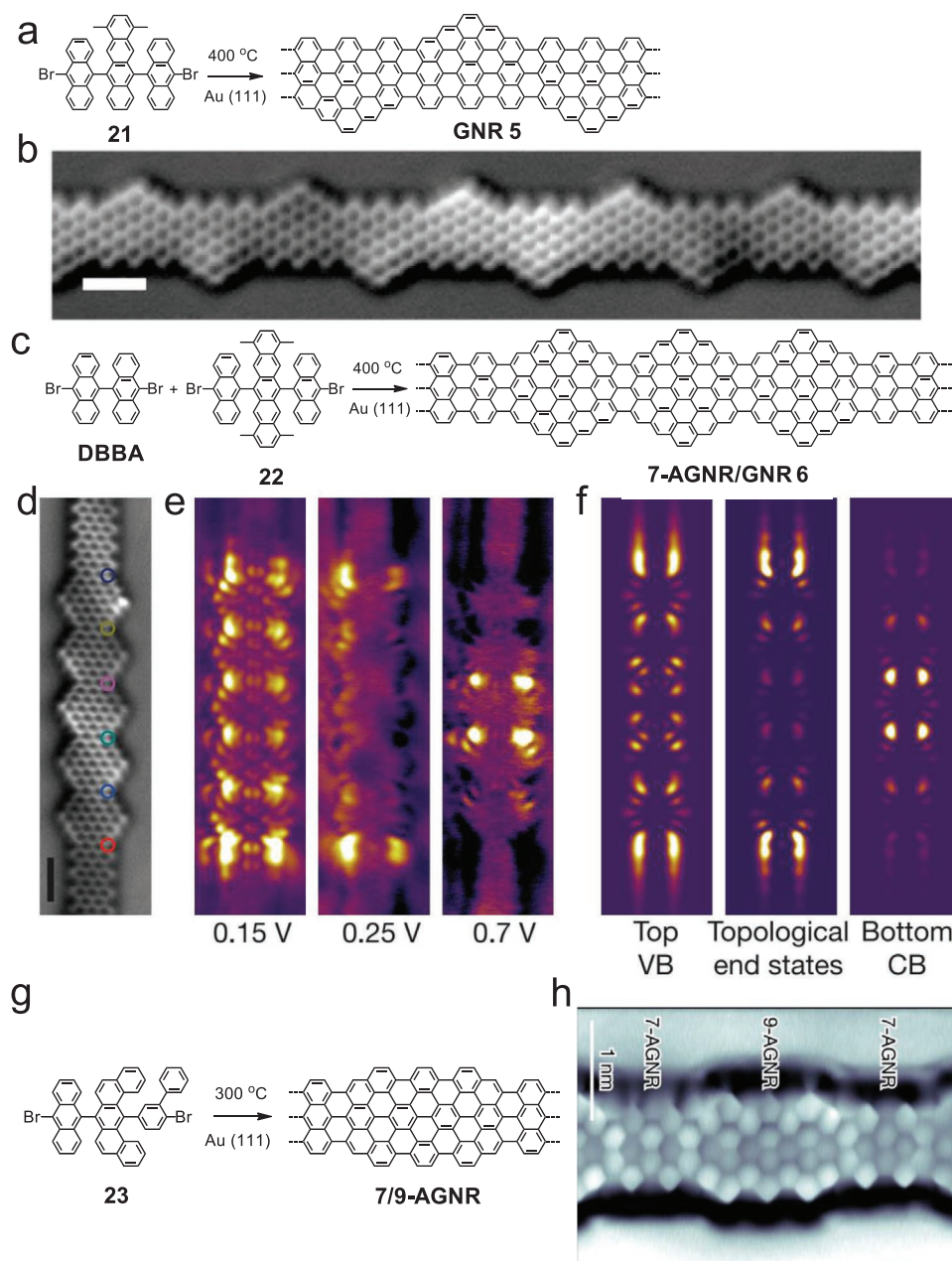


**Figure 7.** a,b) Schematic representation of the on-surface synthesis route from monomer **21** to **GNR 5**, and a typical nc-AFM image. c) On-surface synthesis route for the 7-AGNR backbone extended **GNR 6** and its heterojunction with a 7-AGNR. d) Constant-height nc-AFM frequency shift image of a 7-AGNR/**GNR 6** heterojunction. e) Experimental  $dI/dV$  maps of the main spectroscopic features at +0.15, +0.25, and +0.7 V (all with  $I = 500$  pA). f) Tight-binding simulated charge-density maps at the top of the VB, at  $E = 0$  eV, and at the bottom of the CB, computed for the experimental structure in (d). Scale bar: 1 nm. g) Synthetic route toward a 7/9-AGNR heterojunction. h) Bond-resolved STM image of the 7/9-AGNR heterojunction showing the bond-resolved structure of the heterojunction interface. b,d–f) Reproduced with permission.<sup>[116]</sup> Copyright 2018, Springer Nature. h) Reproduced with permission.<sup>[117]</sup> Copyright 2018, Springer Nature.

the lateral fusion of a short 7-AGNR segment to a long 7-AGNR segment could lead to a 7-14-7 AGNR heterostructure.<sup>[121]</sup> The central 14-AGNR segment with an energy gap of 0.15 eV behaved as a quantum dot connected to two 7-AGNR barriers with a significantly larger energy gap of 2.5 eV. The energy splitting of the interfacial states between the 14-AGNR quantum dot and 7-AGNRs was found to be exponentially dependent on the length. For example, energy splittings of 400 and 80 meV

were found for 14-AGNR quantum dots with lengths of 2 and 10 nm, respectively, suggesting a wide tunability of the fundamental energy gap (Figure 8e,f). Li and co-workers reported the lateral fusion of 7-AGNRs into a 7-14-21 AGNR heterostructure in staircase form.<sup>[122]</sup> In such a staircase heterojunction, the wider 14-AGNR (energy gap:  $\approx 0.3$  eV) and 21-AGNR (energy gap:  $\approx 0.7$  eV) were metallic and small-gap semiconductors, respectively. Therefore, these wide GNRs could serve

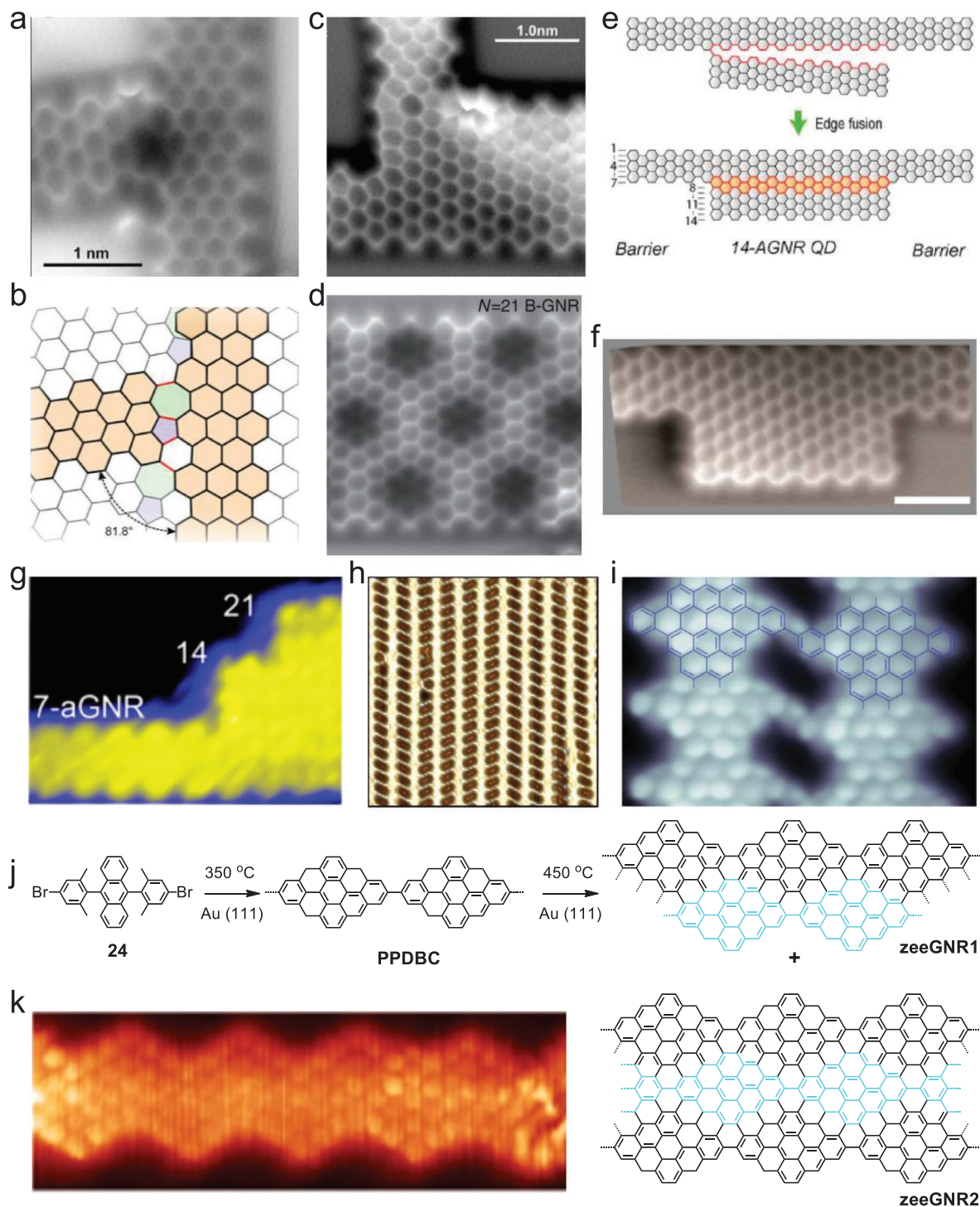


**Figure 8.** a) Constant-height nc-AFM image of a junction between two 7-AGNRs on Au(111). b) Lattice structure of a 7-AGNR junction with four closed bonds (marked in red) in relation to a grain boundary between two graphene domains (graphene lattice in gray). c) Constant-height nc-AFM image of the junction between two 7-AGNRs and one 14-AGNR. d) Constant-height nc-AFM image of a fused  $N = 21$  B-GNR. e) Schematic illustration of the formation of a 14-AGNR quantum dot by edge fusion of two 7-AGNRs. f) nc-AFM image of a short 7-14-7 AGNR quantum dot. Scale bar: 2 nm. g) STM image of a 7-14-21 AGNR staircase heterostructure. h) Laplacian-filtered topographic close-up image of nanoporous graphene. i) CO-functionalized AFM image of nanoporous graphene with the atomic model overlaid. j) Bottom-up on-surface synthesis and fusion of zigzag edge-enriched PPDBC into zeeGNR1 and zeeGNR2. k) STM image of zeeGNR1. a–c) Reproduced with permission.<sup>[120]</sup> Copyright 2015, American Chemical Society. d) Reproduced under the terms of the CC-BY Creative Commons Attribution 4.0 International license (<http://creativecommons.org/licenses/by/4.0>).<sup>[100]</sup> Copyright 2015, Springer Nature. e,f) Reproduced with permission.<sup>[121]</sup> Copyright 2017, American Chemical Society. g) Reproduced with permission.<sup>[122]</sup> Copyright 2017, American Chemical Society. h,i) Reproduced with permission.<sup>[75]</sup> Copyright 2018, American Chemical Society. k) Reproduced with permission.<sup>[126]</sup> Copyright 2019, American Chemical Society.

as electrical contacts to the wide-gap semiconducting 7-AGNR (energy gap:  $\approx 2.6$  eV) to form an all-carbon device with greatly reduced contact barriers (Figure 8g). In addition to 7-AGNRs, 9-AGNRs could also be laterally fused into 18-AGNRs with an energy gap of 0.9 eV.<sup>[77]</sup> On the other hand, poly-*para*-phenylene (PPP), which is formally seen as a 3-AGNR, could also be laterally fused into wider GNRs, thus forming 6-, 9-, 12-, and 15-AGNRs, which showed continuously decreasing bandgaps as they became wider.<sup>[119,123]</sup> Moreover, lateral fusion of PPP with 5- and 7-AGNR could lead to 8- and 10-AGNRs, respectively, which have thus far escaped synthesis due to the lack of suitable precursor molecules.<sup>[124]</sup> Phenyl-functionalized GNRs (see Figure 1b) could be fused and linked together by intermolecular cyclodehydrogenation, which did not form wider GNRs but resulted in atomically precise nanoporous graphene with ordered arrays of nanoscale pores (see Figure 8h,i).<sup>[75,90]</sup> Nanoporous graphene sheets as large as 70 nm were easily obtained, with atomically reproducible pores of  $0.4 \times 0.9$  nm<sup>2</sup>, corresponding to an ultrahigh density of  $4.8 \times 10^5$  pores mm<sup>-2</sup>. An in-plane anisotropic electronic structure was revealed in nanoporous graphene, which contained orthogonal 1D electronic bands with an energy gap of  $\approx 1$  eV. Moreover, the presence of confined states within the nanopores made this material a highly versatile semiconductor for chemical/biological sensing of molecular species.<sup>[75]</sup> An interference Talbot effect (analogous to photons in coupled waveguides) has been predicted for the electrons propagating in such nanoporous graphene because the inter-GNR coupling will disrupt the longitudinal electron confinement in individual channels.<sup>[125]</sup> Recently, zigzag edge-encased poly(*para*-dibenzo[*bc,kl*]-coronene) (PPDBC) was synthesized by polymerization and subsequent cyclodehydrogenation of 9,10-bis(4-bromo-2,6-dimethylphenyl)anthracene (monomer **24**) on a Au(111) surface in UHV.<sup>[126]</sup> Notably, the resulting PPDBC chains can undergo cross-dehydrogenation by thermal annealing at 450 °C, where two or three aligned chains were laterally fused into extended GNRs (zeeGNR1 and zeeGNR2) with a ribbon width of 9 or 17 carbon atoms and an alternating zigzag-armchair periphery in a 6:1 ratio (Figure 8j,k).

## 2.2. On-Surface Synthesis under CVD Conditions

### 2.2.1. Structural Variation of GNRs by the CVD Method

Although atomically precise GNRs with a great variety of structures and properties have been successfully synthesized and visualized under UHV conditions, the accessible amount of GNRs is limited to areas typically smaller than 1 cm<sup>2</sup> due to the limited size of the UHV chamber and/or sample holder, and the elaborate and costly vacuum equipment greatly restricts their large-scale fabrication and further applications.

CVD, as a low-vacuum deposition method, is often used in the semiconductor industry, where gaseous materials are reacted in the vapor phase or on the surface of substrates for the low-cost production of thin films. This method has also been widely employed for the growth of low-dimensional carbon materials, such as carbon nanotubes<sup>[127]</sup> and graphene,<sup>[6,128]</sup> by introducing hydrocarbon gases as carbon sources (such as CH<sub>4</sub>). By employing the readily available CVD setup equipped

with a horizontal tube furnace and a heating belt (see Figure 9a for details), we developed an efficient process for inexpensive and high-throughput synthesis of structurally defined GNRs with varying structures even under ambient-pressure conditions (Figure 9e).<sup>[43]</sup> We thereby utilized the same monomer precursors as in the UHV protocol. In a typical CVD procedure, the monomer was sublimed by the heating belt and deposited on a gold surface inside the horizontal tube furnace, followed by thermal annealing to induce surface-assisted polymerization and then cyclodehydrogenation at higher temperatures (Figure 9a). The CVD method allowed the scaled-up synthesis of chevron-type GNRs and different AGNRs (5-AGNRs, 7-AGNRs, 9-AGNRs, etc.) over large areas of  $>18$  cm<sup>2</sup>, essentially limited only by the furnace and tube dimensions (Figure 9e).<sup>[43–45]</sup> Notably, the Raman spectra of CVD-grown GNRs agreed very well with those of GNRs synthesized under UHV conditions, indicating the high quality of the CVD-grown GNRs. Compared to the UHV approach, trace amounts of oxygen can hardly be excluded in the CVD chamber, which may react with the diradical intermediates, thus terminating the polymerization and leading to shorter and oxidized GNRs. Therefore, hydrogen was mixed with argon in the CVD growth, which was found to be essential to suppress the oxidation, as revealed by high-resolution electron energy loss spectroscopy. High-quality GNRs could thus be achieved only in the presence of hydrogen during the growth, which suppressed the passivation and oxidation of the GNRs by the trace amount of oxygen present during the high-temperature annealing. In addition to pristine GNRs, N-doped and N, S-codoped chevron-type GNRs were further synthesized using nitrogen- and sulfur-containing monomers by the CVD method.<sup>[43]</sup> Moreover, fabrication of GNR heterojunctions, such as p-N-GNRs combining segments of pristine and N-doped GNRs, was also achieved by co-deposition of the monomer and its N-substituted equivalent for CVD growth, where the formation of heterostructures could be confirmed by matrix-assisted laser desorption/ionization time-of-flight mass spectrometry (MALDI-TOF MS) analysis of the polymer precursors.

The CVD growth of GNRs was also demonstrated by Nakae and co-workers under a low pressure ( $\approx 1$  Torr).<sup>[46]</sup> Using molecular precursors, including DBP and DBBA, they reported the fabrication of armchair GNRs such as 5- and 7-AGNRs, respectively.<sup>[46]</sup> In 2017, by using Z-shaped monomer **25**, they further synthesized GNR **7** with a “cove”-type edge in a densely packed array (Figure 10a,b).<sup>[47]</sup> They disclosed a conformation-controlled dehydrogenation procedure where almost perfect dehydrogenation was achieved only for the self-assembled high-density polymers, while polymers deposited at a low density exhibited irregular structures with nonuniform widths.

### 2.2.2. Spectroscopic Characterization of CVD-Grown GNRs

Raman spectroscopy has been widely investigated for the characterization of GNRs and for understanding their electronic structure.<sup>[130]</sup> While atomic-resolution STM images cannot be readily obtained for GNRs fabricated by the CVD method, we could identify different GNRs by Raman spectroscopy, especially in comparison with the spectrum of the same

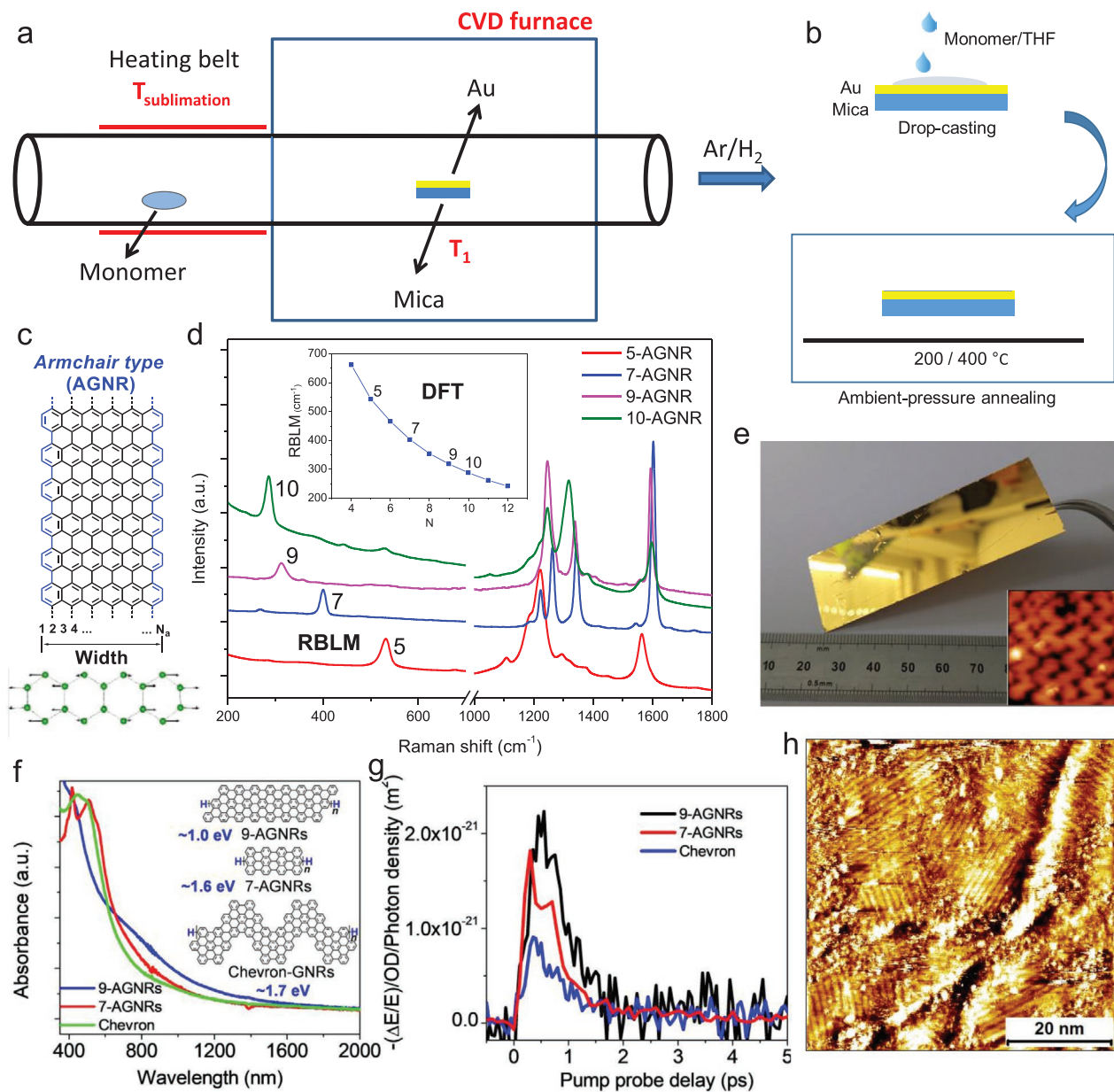


**Figure 9.** a) Schematic illustration of GNR synthesis through CVD. b) Schematic illustration of GNR synthesis through solution processing, which avoids the use of heat and vacuum for monomer deposition. c) Structure of an AGNR, and the atomic displacement characteristics for the RBLM. d) Raman spectra of CVD-grown AGNRs with different widths. The inset shows the calculated RBLM peaks versus GNR width. e) Photograph of a  $25 \times 75 \text{ mm}^2$  GNR/Au/mica plate after GNR growth. The inset presents an STM image of chevron-type GNRs. f) UV-vis-NIR absorption spectra of different CVD-grown GNRs. The inset shows the chemical structures of the GNRs and their optical bandgaps. g) Comparative study of the THz photoconductivity of different GNR structures. h) STM image highlighting domains of 9-AGNRs. a,e) Reproduced with permission.<sup>[43]</sup> Copyright 2016, American Chemical Society. b) Reproduced with permission.<sup>[129]</sup> Copyright 2017, The Chemical Society of Japan. f–h) Reproduced with permission.<sup>[44]</sup> Copyright 2017, American Chemical Society.

GNR prepared under UHV, for which the structure could be directly visualized by STM. Importantly, the radial breathing-like mode (RBLM) of GNRs in the Raman spectra is sensitive to their width and supports the characterization of different CVD-grown GNRs. For example, 5-, 7-, and 9-AGNRs displayed sharp and intense RBLM peaks at 530, 400, and  $315 \text{ cm}^{-1}$ , respectively, which were in excellent agreement with the DFT-calculated RBLM peaks (Figure 9c,d).<sup>[43–45,64,131]</sup> Moreover,

the substantially increased availability of GNRs with the CVD method allowed spectroscopic characterization, such as by UV-vis-NIR absorption and ultrafast terahertz (THz) spectroscopy, by transferring multiple layers of GNRs onto a transparent substrate. We more recently achieved UV-vis-NIR absorption analysis of UHV-grown GNRs in a similar manner,<sup>[132]</sup> but THz spectroscopy of these materials still remains elusive. For multi-layer films of CVD-grown 9-AGNRs, the absorption onset was

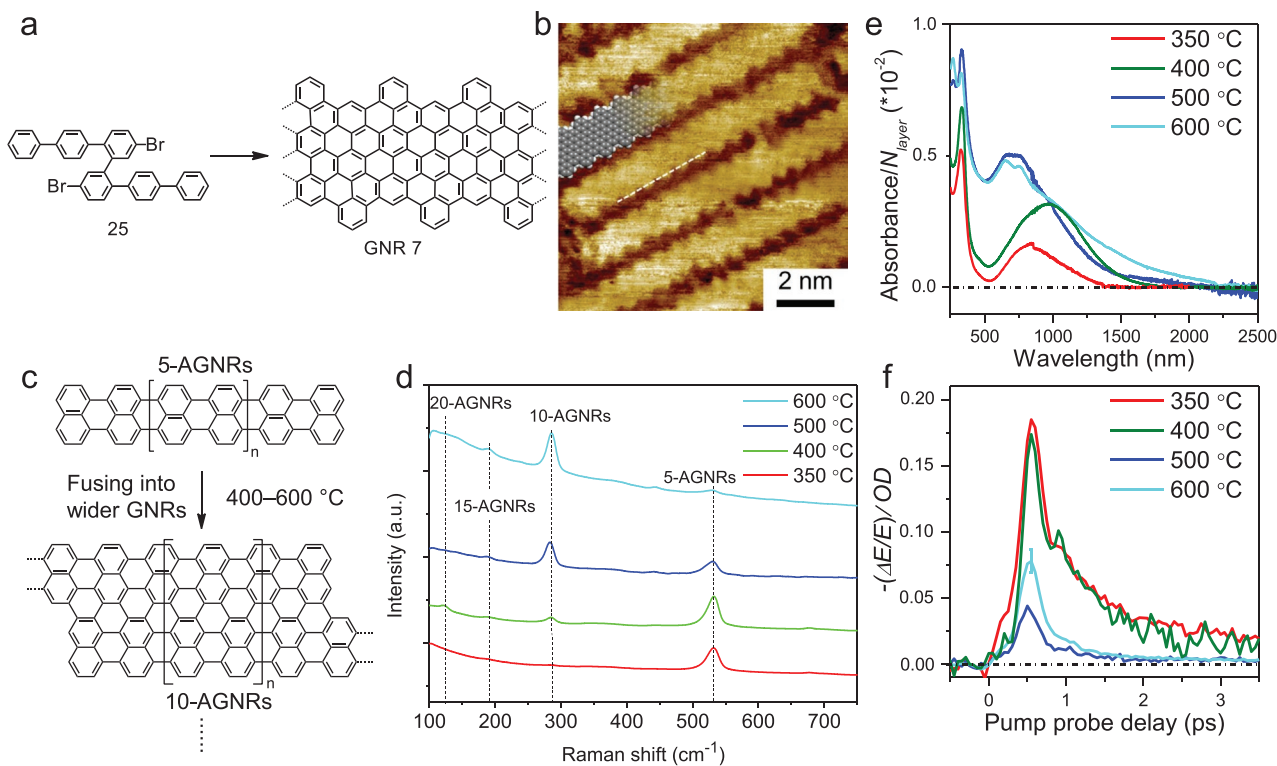


**Figure 10.** On-surface synthesis of GNRs by CVD. a) Synthetic pathway for covalent GNRs with a Z-shaped precursor. b) STM images of a typical covalent GNR on a Au(111) surface. c) Lateral fusion of 5-AGNRs into wider AGNRs. d) Raman spectra of 5-AGNRs annealed at different temperatures showing the RBLM peaks of various extended AGNRs with different widths. e) UV-vis-NIR absorption spectra of extended AGNRs annealed at different temperatures. The spectra are normalized to the number of GNR layers ( $N$  layer). f) Comparative study of the THz photoconductivity of AGNRs annealed at different temperatures. b) Reproduced with permission.<sup>[47]</sup> Copyright 2016, Springer Nature. d-f) Reproduced with permission.<sup>[45]</sup> Copyright 2017, American Chemical Society.

determined to be  $\approx 1200$  nm by extrapolation, suggesting an optical bandgap of  $\approx 1.0$  eV. This was significantly lower than the values obtained for 7-AGNRs ( $\approx 1.6$  eV) and chevron-type GNRs ( $\approx 1.7$  eV) in the same manner (Figure 9f-h).<sup>[44]</sup> Similar values were also reported by the Sakaguchi group for their CVD-fabricated 7- and 9-AGNRs.<sup>[46]</sup> Furthermore, time-resolved THz spectroscopy served as a contact-free and noninvasive approach for the evaluation of the intrinsic photoconductivity within individual GNRs on an ultrashort timescale. The photoconductivity of 9-AGNRs was found to be 1.2 and 2.5 times higher than those of 7-AGNRs and chevron-type GNRs, respectively. This finding displayed the dependence of the conductivity of GNRs on their widths and edge structures and the fact that the photoconductivity was inversely proportional to the optical bandgap. The intrinsic charge-carrier mobility of 9-AGNRs could be calculated to be  $\approx 350$  cm<sup>2</sup> V<sup>-1</sup> s<sup>-1</sup> (Figure 9g), indicating the high potential of such CVD-grown GNRs for electronic device applications.

### 2.2.3. Lateral Fusion of GNRs

In contrast to the local formation of fused GNR segments observed under UHV conditions, we recently found that 5-AGNRs can undergo highly efficient lateral fusion into wider AGNRs, mainly 10-, 15-, and 20-AGNRs, under CVD growth

at higher temperatures ( $>500$  °C) (Figure 10c-f).<sup>[45]</sup> This lateral fusion was clearly evidenced by the appearance of new RBLM peaks at 285, 188, and 122 cm<sup>-1</sup>, which were in excellent agreement with the DFT-calculated RBLM peaks for 10-, 15-, and 20-AGNRs, respectively. The degree of fusion and thus the resulting optical and electronic properties of the resulting GNRs could be controlled by the annealing temperature. When 5-AGNRs were annealed at temperatures ranging from 350 to 400, 500, and 600 °C, the ratio of the Raman RBLM intensities of 10- and 5-AGNRs varied from 0 to 0.1, 1.9, and 10.6, respectively, corroborating the temperature-dependent lateral merging of 5-AGNRs into 10-AGNRs.

The laterally fused GNRs with different widths have totally different band structures. When increasing the annealing temperature, distinct UV-vis-NIR absorption profiles and photoconductivities could be observed. 5-AGNRs annealed at 350 and 400 °C still displayed similar absorption profiles with absorption onsets at 1400 and 1500 nm (corresponding to optical bandgaps of 0.9 and 0.8 eV), respectively, and absorption maxima at 850 and 965 nm, respectively. In contrast, a GNR sample annealed at 500 °C exhibited a significantly different spectrum with two dominant absorption peaks at 650 and 750 nm, which could be assigned to 10-AGNRs based on the theoretical results reported by Prezzi et al.,<sup>[133]</sup> again corroborating the efficient lateral fusion at this temperature. Finally, very broad absorption features extending into the infrared regime up to



≈2250 nm were found for a sample annealed at 600 °C, which could tentatively be attributed to even wider GNRs, including 15- and 20-AGNRs. Such wider low-bandgap GNRs with optical absorption extending from the visible to infrared domain have potential for optoelectronic applications such as visible-to-near infrared sensors. Time-resolved THz spectroscopy provided further insights into the lateral fusion reaction. The GNR samples annealed at 350 and 400 °C displayed the highest THz photoconductivity among all the annealed samples, in agreement with the low-bandgap nature of 5-AGNRs. In contrast, the sample annealed at 500 °C possessed a substantially lower photoconductivity, which could be attributed to the larger bandgap of 10-AGNRs. Annealing at 600 °C increased the photoconductivity in comparison to annealing at 500 °C, consistent with the formation of lower-bandgap 15- and 20-AGNRs.

#### 2.2.4. On-Surface Synthesis of GNRs through Solution Processing of Monomers

In both the CVD and UHV methods, the monomer precursors are deposited by thermal and/or vacuum sublimation, which precludes the use of thermally unstable and/or large monomers that are not sublimable. Recently, we developed a new on-surface synthesis method in which monomers were deposited through solution processing instead of sublimation (Figure 9b).<sup>[129]</sup> In this new method, a monomer precursor solution was drop-cast on a gold surface, forming a thin film of the monomers for subsequent on-surface synthesis of GNRs. The substantial loss of monomers could thus be avoided along with the large energy consumption that occurs during sublimation under heat and vacuum. Subsequent annealing of the monomer film in a tube furnace under ambient pressure (Ar/H<sub>2</sub>) allowed surface-assisted polymerization and cyclodehydrogenation to proceed as in CVD and UHV growth, yielding GNRs with the same structures. Indeed, the Raman spectra of the obtained GNRs were in complete agreement with those of previously reported GNRs synthesized by the CVD and UHV methods, suggesting the high quality and uniformity of the GNRs obtained by the new method. Although shorter lengths of the formed polymers were suggested by MALDI-TOF MS analysis, this on-surface synthesis via solution processing of monomers significantly simplifies the synthesis of GNRs, allowing the scale-up and low-cost production of large-area GNR films for wider applications.

### 3. Recent Advances in the Fabrication of GNR Devices

GNRs hold great promise for the next generation of nano-electronic, spintronic, and optoelectronic devices due to their unique physical properties.<sup>[14,134–136]</sup> Earlier attempts using top-down approaches already demonstrated intriguing properties of GNRs in FET devices.<sup>[20,22,23,137]</sup> However, most GNRs prepared by top-down methods have rough and chemically undefined edge structures that can act as charge traps and hamper carrier transport as well as compromise the unique properties of GNRs, as predicted by theoretical studies, such as those

on the edge states of zigzag GNRs. Moreover, the inability of such methods to accurately control the GNR structures on the atomic scale results in significant sample-to-sample variations in device applications since the electrical, optical, and magnetic properties of GNRs are critically determined by their widths and edge structures, as discussed in the previous sections. Thus, the possibility of tuning the electrical properties of GNRs by controlling their atomically precise structures via rational bottom-up synthesis, together with the high structural and electronic homogeneity, qualifies the bottom-up synthesized GNRs as a much more promising platform for device fabrication and investigations.

In 2014, together with Zhou's group, we achieved the first device based on bottom-up GNRs synthesized by a solution-mediated method.<sup>[138]</sup> The solution-synthesized GNRs could be as long as 600 nm and deposited on a dielectric surface as an isolated strand that allowed the fabrication of single-GNR devices. More devices were subsequently fabricated using solution-synthesized GNRs.<sup>[139–142]</sup> For example, Sinitskii and co-workers utilized thin films of laterally extended chevron-type GNRs for gas sensors that showed improved responsivity to alcohols compared to similar sensors based on graphene.<sup>[92]</sup> On the other hand, the electronic properties expected for such GNRs could not be observed, for example, with a very small  $I_{\text{on}}/I_{\text{off}}$  ratio of up to ≈5 and dominant contact resistance. These results could be partly ascribed to the low homogeneity of the GNR thin films due to their limited dispersibility and strong tendency to aggregate and/or to the insulating alkyl chains that could wrap around the GNRs and induce a large contact resistance between GNRs. To this end, further improvements of the processability and electronic properties of GNRs as well as the device structure and fabrication process can be important, but this discussion is beyond the scope of this article. At present, the GNRs fabricated by surface-assisted synthesis seem to be more favorable for facile device fabrication mainly due to three reasons: 1) the formation of mainly monolayers of pristine GNRs without insulating side groups; 2) the planar conformation of the GNRs on a metal surface, in contrast to the aggregation of GNRs upon deposition from a liquid phase; and 3) the possibility to transfer an intact layer of GNRs from the metal surface onto a dielectric substrate for direct device integration. In this section, we summarize the recent progress in device studies using on-surface synthesized GNRs.

#### 3.1. GNR Transfer Processes

For device fabrication, GNRs grown on a Au/mica substrate must be transferred onto a target substrate with or without the assistance of a polymer film, typically using poly(methyl methacrylate) (PMMA).<sup>[43,46,95,143]</sup> The procedures are similar for both CVD and UHV samples grown on Au/mica substrates, where the only notable differences are the size of the substrate and the density of the GNRs on the surface. For a protocol without the use of PMMA, as-grown GNR/Au/mica substrates were placed on the surface of a hydrofluoric acid solution or a hydrochloric acid solution, which detached the mica and left the Au film with GNRs floating on the surface of the solution. After being washed with ultrapure water, the GNR/Au films were

transferred to new substrates. Finally, the Au films were etched away by a gold etchant, leaving only the GNR films on the new substrates. Nevertheless, due to the fragility of the GNR/Au films, it was difficult to transfer intact GNR films, especially those grown on large substrates. To avoid breaking of the GNR films, PMMA could be used as a mechanical support. PMMA thin films were first spin-coated onto GNR/Au/mica substrates. Then, the mica substrate was removed as described above to furnish the PMMA/GNR/Au film. After etching of the Au film, the PMMA/GNR film could be transferred to a new substrate. The PMMA film was then washed away by hot acetone in the final step, leaving large-area intact GNR films transferred onto the new substrate. However, it is challenging to completely remove PMMA after the transfer, which might compromise some properties of the GNRs, thus affecting the device performance. Therefore, the PMMA-free method appears more favorable if the intended applications are sensitive to the PMMA residue. For device fabrication, the GNR films can be either transferred directly onto predefined electrodes without further treatment or transferred onto a bare substrate followed by a standard photolithography process.

### 3.2. FET Devices Based on UHV-Grown GNRs

In 2013, Bokor and co-workers first reported the transfer of 7-AGNRs prepared under UHV to SiO<sub>2</sub>/Si substrates for fabricating short-channel FET devices.<sup>[143]</sup> The electronic transport was largely dominated by the Schottky barriers at the electrodes, probably due to the narrow width and large bandgap of the GNRs. Nevertheless, a high on/off ratio of  $3.6 \times 10^3$  was observed in the devices with n-type characteristics, as measured under vacuum conditions. To reduce the Schottky barriers and improve the device performance, the use of low-bandgap 9- and 13-AGNRs in short-channel FET devices was explored (Figure 11a–c).<sup>[144]</sup> Both GNRs were grown on Au(111)/mica surfaces under UHV with submonolayer coverage to obtain isolated GNRs and were transferred onto SiO<sub>2</sub>/Si substrates for device fabrication. Using metal electrodes with a 20 nm short channel length and a 50 nm SiO<sub>2</sub> gate dielectric, the resulting GNR-based devices demonstrated ambipolar behavior in their transport characteristics. Tunneling transport, rather than thermionic emission through the Schottky barrier, was found for the devices, as concluded from the weak temperature dependence of the current-voltage characteristics. In contrast to the SiO<sub>2</sub> gate dielectric, transmission through the Schottky barrier was enhanced by gating with an ionic liquid or HfO<sub>2</sub>, resulting in much higher gate efficiency and on-current. In particular, when using a 1.5 nm thick HfO<sub>2</sub> gate dielectric, the 9-AGNR device exhibited excellent switching characteristics with an  $I_{\text{on}}/I_{\text{off}}$  ratio up to  $10^5$  and a high on-current of 1  $\mu\text{A}$  at a drain bias of  $-1$  V. Assuming that most of the current was transported by an individual 9-AGNR, as a submonolayer film with isolated GNRs was used, the normalized conductance could be as high as  $\approx 1000 \mu\text{A} \mu\text{m}^{-1}$  at a  $-1$  V drain bias. Moreover, the normalized conductance was expected to exceed  $20 \text{ mA} \mu\text{m}^{-1}$  in devices using densely aligned GNRs with smaller bandgaps of  $< \approx 1$  eV, where the Schottky barrier could be totally suppressed.<sup>[144]</sup> These results suggest the high potential of UHV-fabricated

GNRs for FET applications. Further improvements of the GNR FET performance require optimization of the GNR bandgap and device configuration. Due to the difficulty in fabricating devices based on GNRs, an in situ electronic measurement technique involving lifting an individual GNR between an STM tip and a Au(111) substrate was developed.<sup>[68,145]</sup> In 2017, Schull and co-workers investigated the electroluminescent properties of an individual 7-AGNR suspended between an STM tip and a Au(111) surface (Figure 11d,e).<sup>[145]</sup> Bright and narrow-band emission of red light was revealed in such GNR/metal junctions based on the STM-induced light emission spectra, and the energy could be tuned by the applied bias voltage. This breakthrough promises a robust route for the realization of controllable graphene-based narrow-band light-emitting devices.

### 3.3. FET Devices Based on CVD-Synthesized GNRs

#### 3.3.1. FET Devices Using Metal Electrodes

Compared with those grown by the UHV method, GNRs grown by the CVD process are much more easily available for devices. In 2014, Sakaguchi et al. first reported the transfer of CVD-synthesized 5-, 7- and 9-AGNRs for FET device studies.<sup>[46]</sup> The devices showed ambipolar transistor behavior with carrier mobilities on the order of  $10^{-6}$  to  $10^{-4} \text{ cm}^2 \text{ V}^{-1} \text{ s}^{-1}$  and an on/off ratio of less than 5. They further demonstrated the use of GNR devices as photovoltaic cells, which showed a 7.3% current gain upon illumination (Figure 12a). In collaboration with Kläu's group, we more recently fabricated FET devices by transferring 5- and 9-AGNR films onto metal electrodes with channel lengths of 500 nm to 5  $\mu\text{m}$  (Figure 12c,d).<sup>[146]</sup> Since the channel length was much greater than the length of the GNRs, the charge carriers crossed the ribbon-ribbon junctions by inter-GNR hopping to form the overall transport current. Indeed, the temperature-dependent charge-transport measurement in a helium bath cryostat verified that the charge-carrier transport in the GNR networks was governed by inter-ribbon hopping mediated by nuclear tunneling. For both 5- and 9-AGNRs, the transport characteristics, which were measured across several orders of magnitude of bias voltages and temperatures ranging from 5 to 262 K, could be combined into a single universal curve describing a nuclear tunneling transport mechanism (Figure 12d). The statistical average hopping lengths for both the 5-AGNR and 9-AGNR were determined to be 17–19 nm, comparable to the average length of individual GNRs in the network based on STM visualization. Therefore, the charge mobility in the GNR network devices was limited by the inter-GNR hopping, and the intrinsic intraribbon mobility could be orders of magnitude larger, as revealed by ultrafast THz spectroscopy.<sup>[44,45]</sup> The use of long GNRs in the network will therefore enable higher field-effect mobilities in GNR-based FET devices. Moreover, transport measurements of these long-channel GNR network FET devices revealed a hysteresis effect in the conductance.<sup>[147]</sup> Temperature-dependent transport measurements suggested that the adsorbed water molecules did not play significant role in the formation of this hysteresis, while the gradually thermally activated shallow traps in the SiO<sub>2</sub> layer dominated the hysteresis effect. Therefore, surface treatment

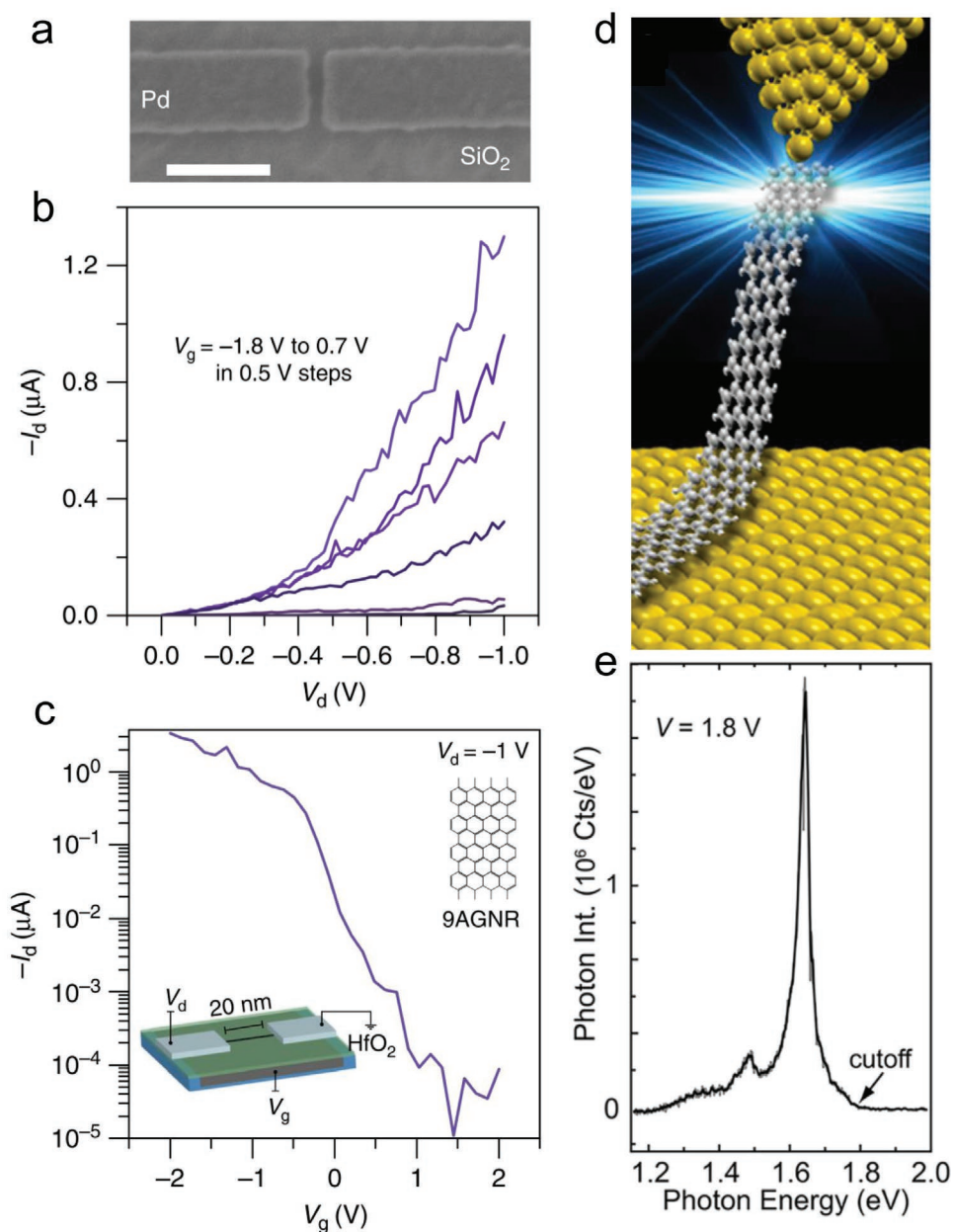


**Figure 11.** a) SEM image of fabricated Pd source–drain electrodes with a 20 nm channel length; scale bar: 100 nm. b)  $I_d$ – $V_d$  and c)  $I_d$ – $V_g$  characteristics of scaled 9-AGNR FET devices with a thin  $\text{HfO}_2$  gate dielectric, showing high  $I_{\text{on}}$  of  $>1 \mu\text{A}$  for a 0.95 nm wide 9-AGNR and a high  $I_{\text{on}}/I_{\text{off}}$  of  $\approx 10^5$ . d) Schematic of the experimental configuration of lifting a single 7-AGNR by an STM tip. e) STM-induced light emission spectra of the suspended ribbon. a–c) Reproduced under the terms of the CC-BY Creative Commons Attribution 4.0 International license (<https://creativecommons.org/licenses/by/4.0/>).<sup>[144]</sup> Copyright 2017, The Authors, published by Springer Nature. d,e) Reproduced with permission.<sup>[145]</sup> Copyright 2017, American Chemical Society.

by passivation of the  $\text{SiO}_2$  surface could reduce the hysteresis effect.

In addition to AGNRs, other kinds of GNRs have been reported for FET device studies. In 2016, we introduced FET devices of CVD-synthesized chevron-type GNRs (Figure 12e,f).<sup>[43]</sup> The  $I_{\text{ds}}$ – $V_{\text{ds}}$  curves suggested p-type conduction and Schottky-contact behavior due to the narrow nature of the GNRs. The superior gate modulation of such long channel devices with a high current on/off ratio of  $>6000$  was significantly higher (more than three orders of magnitude) than that reported thus far for solution-synthesized GNR thin film

network transistors (with typical on/off ratios of  $\approx 2$ – $5$ ).<sup>[138–142]</sup> In 2016, Sakaguchi et al. employed “cove”-type GNR 7 for FET devices, which exhibited ambipolar semiconductor transport with a high mobility of  $0.26 \text{ cm}^2 \text{ V}^{-1} \text{ s}^{-1}$  and an on/off ratio of 88 (Figure 12b).<sup>[47]</sup>

### 3.3.2. FET Devices Using Graphene Electrodes

To avoid the Schottky barriers and screening effect induced by metal electrodes, together with Candini’s group, we further

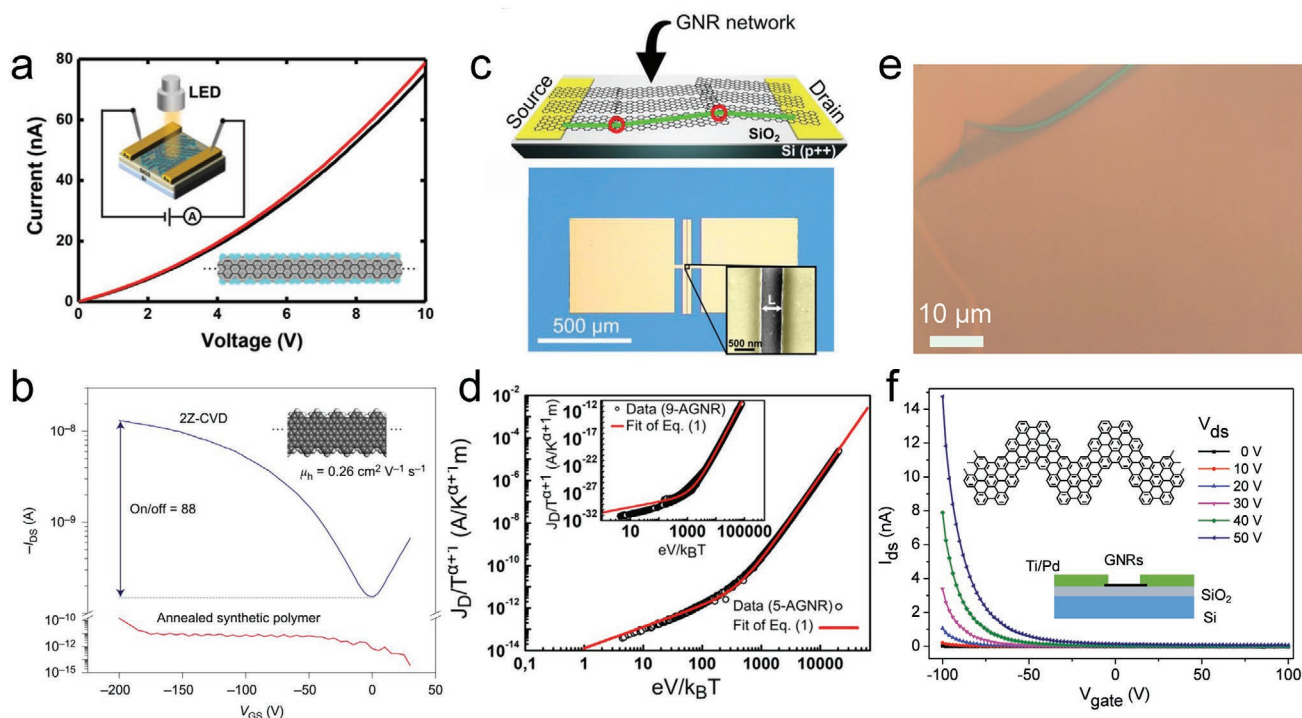


**Figure 12.** a) Effect of white light illumination by an LED on the current–voltage curve and current change of a 5-AGNR film. b) Transfer characteristics of “cove”-type GNRs. c) Schematic depiction of a long-channel GNR network FET, where a possible percolation path is drawn in green. d) Universal scaling curve for 5- and 9-AGNRs. e) Optical microscopy image of a chevron-type GNR film transferred onto a SiO<sub>2</sub>/Si substrate, revealing the uniformity inside the film. f) Transfer curves of a typical chevron-type GNR thin-film transistor measured at different V<sub>ds</sub>, showing unipolar p-type behavior with an on/off current ratio of >1000. a) Reproduced with permission.<sup>[46]</sup> Copyright 2014, Wiley-VCH. b) Reproduced with permission.<sup>[47]</sup> Copyright 2016, Springer Nature. c,d) Reproduced under the terms of the CC-BY Creative Commons Attribution International license (<https://creativecommons.org/licenses/by/4.0/>).<sup>[46]</sup> Copyright 2020, The Authors, published by Springer Nature. e,f) Reproduced with permission.<sup>[43]</sup> Copyright 2016, American Chemical Society.

applied multilayer graphene as the contact electrodes for fabrication of a GNR-based FET, realizing an all-graphene monolithic circuit.<sup>[148]</sup> The channel length of the graphene electrodes, patterned by electron beam lithography and oxygen plasma etching, was ≈100 nm. The contact resistance was significantly reduced, facilitating charge injection, due to the superior GNR/graphene interface (Figure 13a–d). An evident transistor effect with n-type conduction and a current on/off ratio of >100 could be observed. Moreover, this all-graphene FET device was further explored as a sensitive phototransistor.<sup>[148]</sup> Due to the good matching interface between the chevron-type GNR film and the graphene electrodes, the photogenerated carriers could be efficiently extracted from the devices, resulting in a high photosensitivity. The photogenerated current exceeded several tens of nanoamperes in the GNR/graphene devices, which was at least one order of magnitude higher than that measured in previously reported GNR-based devices with metallic electrodes.<sup>[46]</sup> The photocurrent depended on the incident photon power and wavelength. The onset of photocurrent generation at incident photon wavelengths of 650–700 nm corresponded to a photon energy of ≈1.8 eV, which agreed well with the optical bandgap of the GNRs measured by UV–vis–NIR absorption,<sup>[43]</sup> indicating that light absorption by the GNRs was the main mechanism of the photoinduced behavior. A remarkably high photoresponsivity of 5 × 10<sup>5</sup> A W<sup>-1</sup> was observed, which was 8 orders of magnitude higher than that of similar graphene-based devices.<sup>[149]</sup> These results hold promise for an all-graphene system combining

semimetallic graphene with semiconducting GNRs as a viable platform to realize novel devices for optoelectronic applications.

The channel length of the graphene electrodes could be further decreased to 10–50 nm by a modified electroburning procedure,<sup>[150]</sup> similar to the well-known electromigration technique for obtaining atomic break junctions in metals.<sup>[151]</sup> As-fabricated GNRs were directly transferred onto graphene electrodes without further treatment. When the CVD-grown GNR film was transferred to bridge the narrow gap between the graphene electrodes, the number of inter-ribbon junctions was estimated to be <5, and nonlinear and asymmetric behavior of the I<sub>ds</sub>–V<sub>ds</sub> curves was found (Figure 13e–i). p-Type conduction was observed in the devices, with an on/off ratio of typically >10 and the highest value of ≈1000. No significant change was found for the transfer curves operated from 77 to 375 K. The absence of a temperature dependence suggested that the transport mechanism at the injection barrier between the GNRs and the graphene electrodes was dominated by a tunneling (Simmons type) mechanism instead of thermionic emission over the barrier. A high output current was found for 5-AGNRs (up to hundreds of nA with a 1 V applied bias), which was almost two orders of magnitude higher than that for 9-AGNRs. Longer GNRs obtained by UHV growth have also been employed for device investigations, which may increase the contact area and reduce the inter-ribbon junctions. Indeed, the current mean value for 9-AGNRs synthesized in UHV was more than two times that for CVD-grown 9-AGNRs.

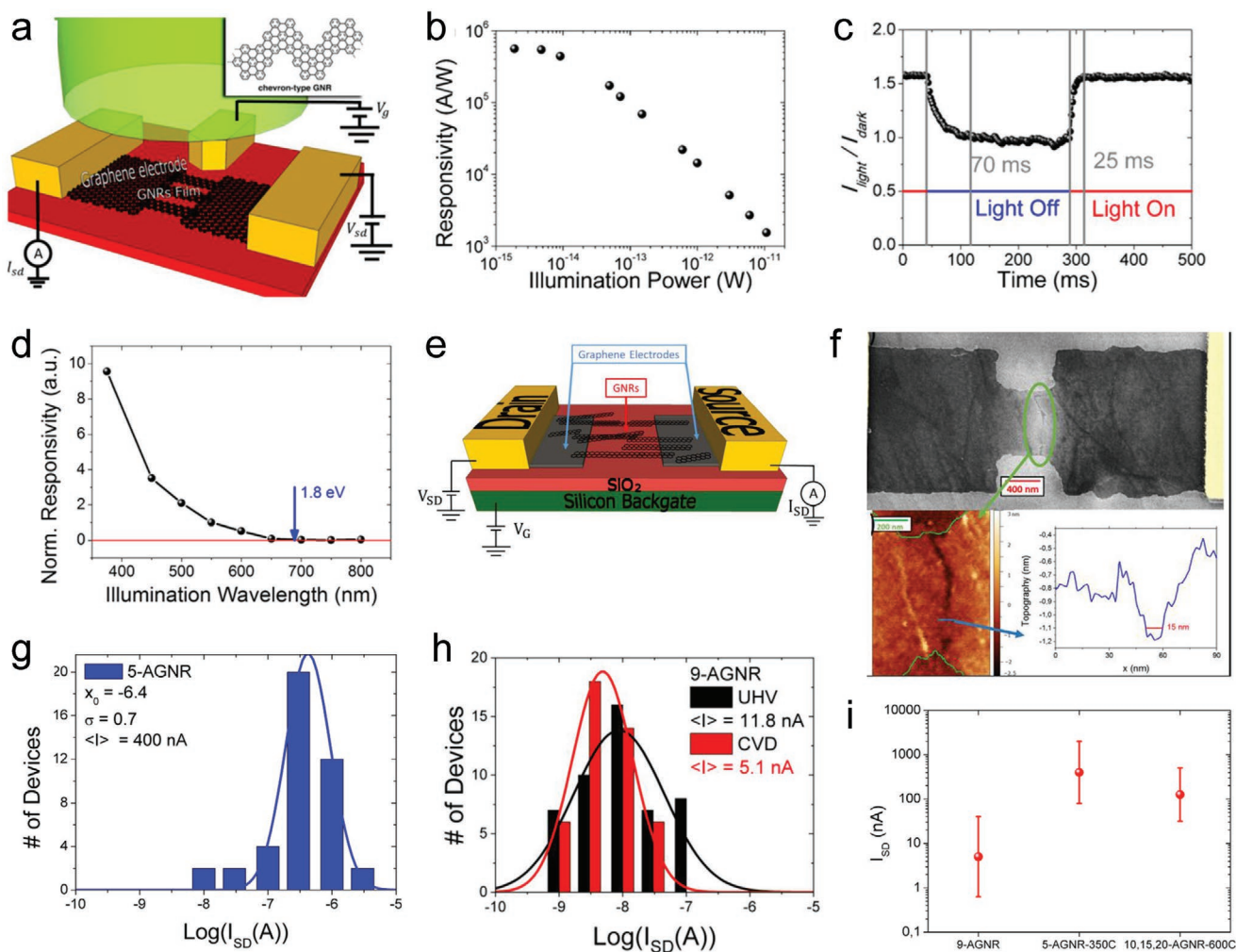


**Figure 13.** a) Schematic view of a phototransistor device consisting of a GNR channel and multilayer epitaxial graphene electrodes. b) Photoresponsivity of the device under monochromatic illumination ( $\lambda = 550$  nm) for different incidence powers. c) Time-resolved photocurrent of the device. d) Normalized photoresponsivity of the device as a function of the photon wavelength  $\lambda$ . e) Schematic view of a short-channel device consisting of two graphene electrodes bridged by one or more AGNRs. f) SEM image and AFM topography image of the device in (e). g) Histograms of the number of 5-AGNR devices with a measured source–drain current  $I_{SD}$  in the corresponding interval ( $V_{SD} = 1$  V;  $V_{Gate} = -50$  V). h) Output current distributions measured for devices based on 9-AGNRs grown with the UHV (black) and CVD (red) methods. i) Output current mean values and standard deviations for three kinds of AGNRs. a–d) Reproduced with permission.<sup>[148]</sup> Copyright 2017, American Chemical Society. e–i) Reproduced with permission.<sup>[150]</sup> Copyright 2019, Elsevier Ltd.

#### 4. Conclusion and Outlook

Tremendous progress has been achieved in the bottom-up on-surface synthesis of GNRs with atomically precise chemical structures under different growth conditions, including UHV and ambient pressure in CVD, by sophisticated design of the monomers. Resulting from the potential of organic chemistry for step-by-step buildup of monomer precursors, tailor-made polymer intermediates could be achieved, whose “graphitization” by the aforementioned strategies paved the way toward the synthesis of atomically precise GNRs with diverse structures. This is in stark contrast to single-wall carbon nanotubes (SWCNTs), whose chirality-selective synthesis still remains the top challenge in the field, and contamination with metallic SWCNTs highly compromises the device applications of semiconducting SWCNTs.<sup>[152,153]</sup> Despite this great success, the UHV protocol still has room for

further developments. For example, the current on-surface synthesis heavily relies on the Ullmann-type homocoupling reaction, allowing only AA-type polymerization, while selective heterocoupling and AB-type polymerization on the surface still remain a challenge. Selective AB-type polymerization would greatly expand the scope of possible GNR structures. On-surface heterocoupling would also enable  $A_2B_2$ -type polymerization, selectively leading to GNR heterostructures combining, for example, electron-rich and electron-poor segments in an alternating manner. Moreover, further development of the on-surface reactions, e.g., not limited to the use of halides for polymerization, is also essential for achieving a wider variety of GNRs with novel structures. The recent development of novel on-surface reactions such as azomethine ylide homocoupling<sup>[154]</sup> and covalent C–N bond formation by mild thermally induced oxidative cyclodehydrogenation<sup>[155]</sup> may open new opportunities for internally N-doping of GNRs.

On the other hand, the on-surface synthesis under CVD conditions relaxes the rigorous UHV conditions and substantially simplifies the procedure, leading to low-cost and large-area production of GNRs. The larger amount of GNRs available with the CVD method facilitates, for example, the transfer of multilayers of GNRs for spectroscopic characterization, such as by UV-vis-NIR absorption and THz spectroscopy, which require many layers of GNRs to reach sufficient optical densities. The CVD method is also industrially viable and more promising for real-world applications of GNRs. Nevertheless, the CVD conditions need to be further improved to, for example, produce longer GNRs, as achieved by the UHV protocol. Moreover, the variety of GNRs that can be synthesized under CVD conditions is significantly limited compared with that under UHV conditions since unstable monomers, polymer precursors, and/or GNRs, such as ZGNRs, can be heavily oxidized and most likely decomposed. One possible approach to this challenge is edge “passivation” since functionalization of zigzag edges with, for example, ethylene<sup>[156]</sup> or iodine<sup>[157]</sup> has been proposed to reduce the chemical reactivity while preserving the localized states at the zigzag edges. Incorporation of heteroatoms might also improve the stability while partly maintaining the edge states and simultaneously tuning the electronic properties of ZGNRs. Such edge “passivation” and heteroatom doping should be vital for the future applications of ZGNRs.

Significant steps toward GNR devices have been made by transferring on-surface-synthesized GNRs onto insulating substrates from a metal surface. Since the GNRs flatly lie on the surface after growth, direct transfer of the GNR film can achieve face-on deposition of GNRs on insulating substrates, which is favorable for integration into FET devices. Nevertheless, increasing the length of the GNRs is one of the most urgent synthetic targets for facilitating device fabrication and reducing the contact resistance with electrodes. Moreover, the development of GNR synthesis on nonmetal substrates is highly important to avoid the transfer process, which could cause undesired contamination and/or deterioration of the GNRs. One possible approach could be to devise a synthetic route based only on thermally induced reactions without the need of metal catalysis. Transport in most of the reported GNR devices was largely dominated by Schottky barriers, which was ascribed to their small width and large bandgaps, precluding the access to their intrinsic transport properties. Thus, the design of a monomer that can lead to stable GNRs with a lower bandgap is in high demand. Indeed, FET devices with much higher on-currents have been achieved in the low-bandgap 5- and 9-AGNRs due to their lower effective mass and smaller Schottky barriers. One of the next device-driven challenges in the synthesis is selective synthesis of wider AGNRs with even lower bandgaps, for example, those in the  $3n+2$  family, such as 8- and 11-AGNRs. High-density parallel alignment of low-bandgap GNRs would furnish long-awaited semiconductors for FETs, which would allow multichannel transport with higher current thresholds. The use of graphene rather than metal as the contact electrodes has also been found to be an effective way to reduce the Schottky barriers and contact resistance. The next open question is whether the ends of GNRs can be covalently bonded or even fused with the edges of graphene electrodes to further improve the charge transport to obtain a

higher performance in devices. The other device configurations using ionic liquid as gating and  $\text{HfO}_2$  as dielectric have been shown to effectively boost the on-current and on/off ratio. Further exploration of new device structures and their optimization for the GNRs can be an important factor to improve the performance of GNR-based devices. Further, the abovementioned edge “passivation” and heteroatom doping of the zigzag edges might allow for device integration of ZGNRs with magnetic edge states for spintronics device applications. Thus, further developments in new GNR structures are expected to overcome the inherent limitations of graphene and carbon nanotubes and qualify them as unique components for future (opto)electronics and many other applications.

## Acknowledgements

The authors thank all their distinguished collaboration partners and dedicated colleagues, who enabled the achievements partly described in this article. They also appreciate the support from the Max Planck Society, the National Program for Thousand Young Talents of China, the Fundamental Research Funds for the Central Universities (No. 2019QNA4008), the National Science Foundation of China (No. 51902285), the EU Projects through the FET-Proactive Project “MoQuaS” (No. 610449), the Graphene Flagship (No. CNECT-ICT-604391), the Horizon 2020 research and innovation programme GrapheneCore1 (696656), the European Research Council (ERC)-Adv.-Grant 267160 (NANOGRAPH), and the Office of Naval Research Basic Research Challenge (BRC) Program (molecular synthesis and characterization).

Open access funding enabled and organized by Projekt DEAL.

## Conflict of Interest

The authors declare no conflict of interest.

## Keywords

chemical vapor deposition, graphene nanoribbons, on-surface synthesis, ultrahigh vacuum

Received: March 18, 2020

Revised: June 1, 2020

Published online: September 18, 2020

- [1] K. S. Novoselov, A. K. Geim, S. V. Morozov, D. Jiang, Y. Zhang, S. V. Dubonos, I. V. Grigorieva, A. A. Firsov, *Science* **2004**, 306, 666.
- [2] K. I. Bolotin, K. J. Sikes, Z. Jiang, M. Klima, G. Fudenberg, J. Hone, P. Kim, H. L. Stormer, *Solid State Commun.* **2008**, 146, 351.
- [3] E. Pop, V. Varshney, A. K. Roy, *MRS Bull.* **2012**, 37, 1273.
- [4] C. Lee, X. Wei, J. W. Kysar, J. Hone, *Science* **2008**, 321, 385.
- [5] F. Bonaccorso, L. Colombo, G. Yu, M. Stoller, V. Tozzini, A. C. Ferrari, R. S. Ruoff, V. Pellegrini, *Science* **2015**, 347, 1246501.
- [6] A. Reina, X. T. Jia, J. Ho, D. Nezich, H. B. Son, V. Bulovic, M. S. Dresselhaus, J. Kong, *Nano Lett.* **2009**, 9, 30.
- [7] F. Bonaccorso, Z. Sun, T. Hasan, A. C. Ferrari, *Nat. Photonics* **2010**, 4, 611.
- [8] A. H. Castro Neto, F. Guinea, N. M. R. Peres, K. S. Novoselov, A. K. Geim, *Rev. Mod. Phys.* **2009**, 81, 109.
- [9] V. N. Kotov, B. Uchoa, V. M. Pereira, F. Guinea, A. H. Castro Neto, *Rev. Mod. Phys.* **2012**, 84, 1067.
- [10] L. Talirz, P. Ruffieux, R. Fasel, *Adv. Mater.* **2016**, 28, 6222.

- [11] A. Narita, X. Y. Wang, X. L. Feng, K. Müllen, *Chem. Soc. Rev.* **2015**, 44, 6616.
- [12] A. Narita, Z. P. Chen, Q. Chen, K. Müllen, *Chem. Sci.* **2019**, 10, 964.
- [13] V. Barone, O. Hod, G. E. Scuseria, *Nano Lett.* **2006**, 6, 2748.
- [14] Y. W. Son, M. L. Cohen, S. G. Louie, *Phys. Rev. Lett.* **2006**, 97, 216803.
- [15] L. Yang, C. H. Park, Y. W. Son, M. L. Cohen, S. G. Louie, *Phys. Rev. Lett.* **2007**, 99, 186801.
- [16] J. Wang, R. Zhao, M. Yang, Z. Liu, Z. Liu, *J. Chem. Phys.* **2013**, 138, 084701.
- [17] S. A. Wolf, D. D. Awschalom, R. A. Buhrman, J. M. Daughton, S. von Molnar, M. L. Roukes, A. Y. Chtchelkanova, D. M. Treger, *Science* **2001**, 294, 1488.
- [18] N. Mohanty, D. Moore, Z. Xu, T. S. Sreeprasad, A. Nagaraja, A. A. Rodriguez, V. Berry, *Nat. Commun.* **2012**, 3, 844.
- [19] L. Tapasztó, G. Dobrik, P. Lambin, L. P. Biro, *Nat. Nanotechnol.* **2008**, 3, 397.
- [20] M. Y. Han, B. Ozyilmaz, Y. Zhang, P. Kim, *Phys. Rev. Lett.* **2007**, 98, 206805.
- [21] Z. Chen, Y.-M. Lin, M. J. Rooks, P. Avouris, *Phys. E* **2007**, 40, 228.
- [22] X. L. Li, X. R. Wang, L. Zhang, S. W. Lee, H. J. Dai, *Science* **2008**, 319, 1229.
- [23] L. Y. Jiao, L. Zhang, X. R. Wang, G. Diankov, H. J. Dai, *Nature* **2009**, 458, 877.
- [24] D. V. Kosynkin, A. L. Higginbotham, A. Sinitskii, J. R. Lomeda, A. Dimiev, B. K. Price, J. M. Tour, *Nature* **2009**, 458, 872.
- [25] A. Narita, X. L. Feng, K. Müllen, *Chem. Rec.* **2015**, 15, 295.
- [26] L. Chen, Y. Hernandez, X. Feng, K. Müllen, *Angew. Chem., Int. Ed.* **2012**, 51, 7640.
- [27] J. S. Wu, L. Gherghel, M. D. Watson, J. X. Li, Z. H. Wang, C. D. Simpson, U. Kolb, K. Müllen, *Macromolecules* **2003**, 36, 7082.
- [28] Y. Fogel, L. J. Zhi, A. Rouhanipour, D. Andrienko, H. J. Rader, K. Müllen, *Macromolecules* **2009**, 42, 6878.
- [29] A. Narita, X. L. Feng, Y. Hernandez, S. A. Jensen, M. Bonn, H. F. Yang, I. A. Verzhbitskiy, C. Casiraghi, M. R. Hansen, A. H. R. Koch, G. Fytas, O. Ivasenko, B. Li, K. S. Mali, T. Balandina, S. Mahesh, S. De Feyter, K. Müllen, *Nat. Chem.* **2014**, 6, 126.
- [30] A. Narita, I. A. Verzhbitskiy, W. Frederickx, K. S. Mali, S. A. Jensen, M. R. Hansen, M. Bonn, S. De Feyter, C. Casiraghi, X. Feng, K. Müllen, *ACS Nano* **2014**, 8, 11622.
- [31] M. G. Schwab, A. Narita, Y. Hernandez, T. Balandina, K. S. Mali, S. De Feyter, X. L. Feng, K. Müllen, *J. Am. Chem. Soc.* **2012**, 134, 18169.
- [32] T. H. Vo, M. Shekhirev, D. A. Kunkel, M. D. Morton, E. Berglund, L. M. Kong, P. M. Wilson, P. A. Dowben, A. Enders, A. Sinitskii, *Nat. Commun.* **2014**, 5, 3189.
- [33] Y. Yano, N. Mitoma, K. Matsushima, F. J. Wang, K. Matsui, A. Takakura, Y. Miyauchi, H. Ito, K. Itami, *Nature* **2019**, 571, 387.
- [34] N. Mitoma, Y. Yano, H. Ito, Y. Miyauchi, K. Itami, *ACS Appl. Nano Mater.* **2019**, 2, 4825.
- [35] T. H. Vo, M. Shekhirev, D. A. Kunkel, M. D. Morton, E. Berglund, L. Kong, P. M. Wilson, P. A. Dowben, A. Enders, A. Sinitskii, *Nat. Commun.* **2014**, 5, 3189.
- [36] Y.-Z. Tan, B. Yang, K. Parvez, A. Narita, S. Osella, D. Beljonne, X. Feng, K. Müllen, *Nat. Commun.* **2013**, 4, 2646.
- [37] A. Keerthi, B. Radha, D. Rizzo, H. Lu, V. Diez Cabanes, I. C. Hou, D. Beljonne, J. Cornil, C. Casiraghi, M. Baumgarten, K. Müllen, A. Narita, *J. Am. Chem. Soc.* **2017**, 139, 16454.
- [38] F. Xu, C. Yu, A. Tries, H. Zhang, M. Kläui, K. Basse, M. R. Hansen, N. Bilbao, M. Bonn, H. I. Wang, Y. Mai, *J. Am. Chem. Soc.* **2019**, 141, 10972.
- [39] W. Yang, A. Lucotti, M. Tommasini, W. A. Chalifoux, *J. Am. Chem. Soc.* **2016**, 138, 9137.
- [40] Y. J. Huang, F. G. Xu, L. Ganzer, F. V. A. Camargo, T. Nagahara, J. Teyssandier, H. Van Gorp, K. Basse, L. A. Straaso, V. Nagyte, C. Casiraghi, M. R. Hansen, S. De Feyter, D. Y. Yan, K. Muellen, X. L. Feng, G. Cerullo, Y. Y. Mai, *J. Am. Chem. Soc.* **2018**, 140, 10416.
- [41] M. Slota, A. Keerthi, W. K. Myers, E. Tretyakov, M. Baumgarten, A. Ardavan, H. Sadeghi, C. J. Lambert, A. Narita, K. Müllen, L. Bogani, *Nature* **2018**, 557, 691.
- [42] A. Fairbrother, J. R. Sanchez-Valencia, B. Lauber, I. Shorubalko, P. Ruffieux, T. Hintermann, R. Fasel, *Nanoscale* **2017**, 9, 2785.
- [43] Z. Chen, W. Zhang, C.-A. Palma, A. Lodi Rizzini, B. Liu, A. N. Abbas, N. Richter, L. Martini, X.-Y. Wang, N. Cavani, H. Lu, N. Mishra, C. Coletti, R. Berger, F. Klappenberger, M. Kläui, A. Candini, M. Affronte, C. Zhou, V. De Renzi, U. del Pennino, J. V. Barth, H. J. Räder, A. Narita, X. Feng, K. Müllen, *J. Am. Chem. Soc.* **2016**, 138, 15488.
- [44] Z. Chen, H. I. Wang, J. Teyssandier, K. S. Mali, T. Dumschlaff, I. Ivanov, W. Zhang, P. Ruffieux, R. Fasel, H. J. Räder, D. Turchinovich, S. De Feyter, X. Feng, M. Kläui, A. Narita, M. Bonn, K. Müllen, *J. Am. Chem. Soc.* **2017**, 139, 3635.
- [45] Z. Chen, H. I. Wang, N. Bilbao, J. Teyssandier, T. Prechtel, N. Cavani, A. Tries, R. Biagi, V. De Renzi, X. Feng, M. Kläui, S. De Feyter, M. Bonn, A. Narita, K. Müllen, *J. Am. Chem. Soc.* **2017**, 139, 9483.
- [46] H. Sakaguchi, Y. Kawagoe, Y. Hirano, T. Iruka, M. Yano, T. Nakae, *Adv. Mater.* **2014**, 26, 4134.
- [47] H. Sakaguchi, S. Song, T. Kojima, T. Nakae, *Nat. Chem.* **2017**, 9, 57.
- [48] L. Gao, W. Ren, H. Xu, L. Jin, Z. Wang, T. Ma, L. P. Ma, Z. Zhang, Q. Fu, L. M. Peng, X. Bao, H. M. Cheng, *Nat. Commun.* **2012**, 3, 699.
- [49] X.-Y. Wang, A. Narita, K. Müllen, *Nat. Rev. Mater.* **2017**, 2, 0100.
- [50] N. Richter, Z. Chen, M.-L. Braatz, F. Musseau, N.-E. Weber, A. Narita, K. Müllen, M. Kläui, *Ann. Phys.* **2017**, 529, 1700051.
- [51] I. C.-Y. Hou, Y. Hu, A. Narita, K. Müllen, *Polym. J.* **2018**, 50, 3.
- [52] S. Kawai, *Polym. J.* **2017**, 49, 3.
- [53] P. H. Jacobse, M. E. Moret, R. J. M. K. Gebbink, I. Swart, *Synlett* **2017**, 28, 2509.
- [54] Y. Segawa, H. Ito, K. Itami, *Nat. Rev. Mater.* **2016**, 1, 15002.
- [55] Y. Yano, N. Mitoma, H. Ito, K. Itami, *J. Org. Chem.* **2020**, 85, 4.
- [56] X. Zhou, G. Yu, *Adv. Mater.* **2020**, 32, 1905957.
- [57] J. M. Cai, P. Ruffieux, R. Jaafar, M. Bieri, T. Braun, S. Blankenburg, M. Muoth, A. P. Seitsonen, M. Saleh, X. L. Feng, K. Müllen, R. Fasel, *Nature* **2010**, 466, 470.
- [58] P. Han, K. Akagi, F. Federici Canova, H. Mutoh, S. Shiraki, K. Iwaya, P. S. Weiss, N. Asao, T. Hitosugi, *ACS Nano* **2014**, 8, 9181.
- [59] C. Sanchez-Sanchez, T. Dienel, O. Deniz, P. Ruffieux, R. Berger, X. L. Peng, K. Müllen, R. Fasel, *ACS Nano* **2016**, 10, 8006.
- [60] P. Han, K. Akagi, F. F. Canova, R. Shimizu, H. Oguchi, S. Shiraki, P. S. Weiss, N. Asao, T. Hitosugi, *ACS Nano* **2015**, 9, 12035.
- [61] D. G. de Oteyza, A. García-Lekue, M. Vilas-Varela, N. Merino-Díez, E. Carbonell-Sanromà, M. Corso, G. Vasseur, C. Rogero, E. Guitián, J. I. Pascual, J. E. Ortega, Y. Wakayama, D. Peña, *ACS Nano* **2016**, 10, 9000.
- [62] P. H. Jacobse, A. van den Hoogenband, M.-E. Moret, R. J. M. Klein Gebbink, I. Swart, *Angew. Chem., Int. Ed.* **2016**, 55, 13052.
- [63] C. Moreno, M. Paradinas, M. Vilas-Varela, M. Panighel, G. Ceballos, D. Pena, A. Mugarza, *Chem. Commun.* **2018**, 54, 9402.
- [64] L. Talirz, H. Sode, T. Dumschlaff, S. Wang, J. R. Sanchez-Valencia, J. Liu, P. Shinde, C. A. Pignedoli, L. Liang, V. Meunier, N. C. Plumb, M. Shi, X. Feng, A. Narita, K. Müllen, R. Fasel, P. Ruffieux, *ACS Nano* **2017**, 11, 1380.
- [65] M. Di Giovannantonio, O. Deniz, J. I. Urgel, R. Widmer, T. Dienel, S. Stolz, C. Sánchez-Sánchez, M. Muntwiler, T. Dumschlaff, R. Berger, A. Narita, X. Feng, K. Müllen, P. Ruffieux, R. Fasel, *ACS Nano* **2018**, 12, 74.
- [66] Y. C. Chen, D. G. de Oteyza, Z. Pedramrazi, C. Chen, F. R. Fischer, M. F. Crommie, *ACS Nano* **2013**, 7, 6123.
- [67] P. Ruffieux, J. Cai, N. C. Plumb, L. Patthey, D. Prezzi, A. Ferretti, E. Molinari, X. Feng, K. Müllen, C. A. Pignedoli, R. Fasel, *ACS Nano* **2012**, 6, 6930.

- [68] M. Koch, F. Ample, C. Joachim, L. Grill, *Nat. Nanotechnol.* **2012**, *7*, 713.
- [69] H. Söde, L. Talirz, O. Gröning, C. A. Pignedoli, R. Berger, X. Feng, K. Müllen, R. Fasel, P. Ruffieux, *Phys. Rev. B* **2015**, *91*, 045429.
- [70] H. Zhang, H. Lin, K. Sun, L. Chen, Y. Zagranyski, N. Aghdassi, S. Duhm, Q. Li, D. Zhong, Y. Li, K. Müllen, H. Fuchs, L. Chi, *J. Am. Chem. Soc.* **2015**, *137*, 4022.
- [71] A. Kimouche, M. M. Ervasti, R. Drost, S. Halonen, A. Harju, P. M. Joensuu, J. Sainio, P. Liljeroth, *Nat. Commun.* **2015**, *6*, 10177.
- [72] L. Talirz, H. Söde, S. Kawai, P. Ruffieux, E. Meyer, X. Feng, K. Müllen, R. Fasel, C. A. Pignedoli, D. Passerone, *ChemPhysChem* **2019**, *20*, 2348.
- [73] P. H. Jacobse, K. A. Simonov, M. J. J. Mangnus, G. I. Svirskiy, A. V. Generalov, A. S. Vinogradov, A. Sandell, N. Mårtensson, A. B. Preobrajenski, I. Swart, *J. Phys. Chem. C* **2019**, *123*, 8892.
- [74] S. Linden, D. Zhong, A. Timmer, N. Aghdassi, J. H. Franke, H. Zhang, X. Feng, K. Müllen, H. Fuchs, L. Chi, H. Zacharias, *Phys. Rev. Lett.* **2012**, *108*, 216801.
- [75] C. Moreno, M. Vilas-Varela, B. Kretz, A. Garcia-Lekue, M. V. Costache, M. Paradinas, M. Panighel, G. Ceballos, S. O. Valenzuela, D. Peña, A. Mugarza, *Science* **2018**, *360*, 199.
- [76] Y. C. Chen, T. Cao, C. Chen, Z. Pedramrazi, D. Haberer, D. G. de Oteyza, F. R. Fischer, S. G. Louie, M. F. Crommie, *Nat. Nanotechnol.* **2015**, *10*, 156.
- [77] O. Deniz, C. Sánchez-Sánchez, T. Dumschlaff, X. Feng, A. Narita, K. Müllen, N. Kharche, V. Meunier, R. Fasel, P. Ruffieux, *Nano Lett.* **2017**, *17*, 2197.
- [78] J. B. Neaton, M. S. Hybertsen, S. G. Louie, *Phys. Rev. Lett.* **2006**, *97*, 216405.
- [79] N. Kharche, V. Meunier, *J. Phys. Chem. Lett.* **2016**, *7*, 1526.
- [80] C. X. Ma, Z. C. Xiao, H. H. Zhang, L. B. Liang, J. S. Huang, W. C. Lu, B. G. Sumpter, K. L. Hong, J. Bernholc, A. P. Li, *Nat. Commun.* **2017**, *8*, 14815.
- [81] S. Y. Wang, L. Talirz, C. A. Pignedoli, X. L. Feng, K. Müllen, R. Fasel, P. Ruffieux, *Nat. Commun.* **2016**, *7*, 11507.
- [82] P. Ruffieux, S. Wang, B. Yang, C. Sánchez-Sánchez, J. Liu, T. Dienel, L. Talirz, P. Shinde, C. A. Pignedoli, D. Passerone, T. Dumschlaff, X. Feng, K. Müllen, R. Fasel, *Nature* **2016**, *531*, 489.
- [83] C. Sánchez-Sánchez, T. Dienel, A. Nicolaï, N. Kharche, L. Liang, C. Daniels, V. Meunier, J. Liu, X. Feng, K. Müllen, J. R. Sánchez-Valencia, O. Gröning, P. Ruffieux, R. Fasel, *Chem. - Eur. J.* **2019**, *25*, 12074.
- [84] Q. Fan, D. Martin-Jimenez, D. Ebeling, C. K. Krug, L. Brechmann, C. Kohlmeier, G. Hilt, W. Hieringer, A. Schirmeisen, J. M. Gottfried, *J. Am. Chem. Soc.* **2019**, *141*, 17713.
- [85] X.-Y. Wang, J. I. Urgel, G. B. Barin, K. Eimre, M. Di Giovannantonio, A. Milani, M. Tommasini, C. A. Pignedoli, P. Ruffieux, X. L. Feng, R. Fasel, K. Müllen, A. Narita, *J. Am. Chem. Soc.* **2018**, *140*, 9104.
- [86] M. Z. Liu, M. X. Liu, L. M. She, Z. Q. Zha, J. L. Pan, S. C. Li, T. Li, Y. Y. He, Z. Y. Cai, J. B. Wang, Y. Zheng, X. H. Qiu, D. Y. Zhong, *Nat. Commun.* **2017**, *8*, 14924.
- [87] R. Denk, A. Lodi-Rizzini, S. Wang, M. Hohage, P. Zeppenfeld, J. Cai, R. Fasel, P. Ruffieux, R. F. J. Berger, Z. Chen, A. Narita, X. Feng, K. Müllen, R. Biagi, V. De Renzi, D. Prezzi, A. Ruini, A. Ferretti, *Nanoscale* **2017**, *9*, 18326.
- [88] J. D. Teeter, P. S. Costa, M. M. Pour, D. P. Miller, E. Zurek, A. Enders, A. Sinitskii, *Chem. Commun.* **2017**, *53*, 8463.
- [89] J. D. Teeter, P. Zahl, M. Mehdi Pour, P. S. Costa, A. Enders, A. Sinitskii, *ChemPhysChem* **2019**, *20*, 2281.
- [90] M. Shekhirev, P. Zahl, A. Sinitskii, *ACS Nano* **2018**, *12*, 8662.
- [91] P. S. Costa, J. D. Teeter, A. Enders, A. Sinitskii, *Carbon* **2018**, *134*, 310.
- [92] M. Mehdi Pour, A. Lashkov, A. Radocea, X. Liu, T. Sun, A. Lipatov, R. A. Korlacki, M. Shekhirev, N. R. Aluru, J. W. Lyding, V. Sysoev, A. Sinitskii, *Nat. Commun.* **2017**, *8*, 820.
- [93] J. Z. Liu, B. W. Li, Y. Z. Tan, A. Giannakopoulos, C. Sanchez-Sanchez, D. Beljonne, P. Ruffieux, R. Fasel, X. L. Feng, K. Müllen, *J. Am. Chem. Soc.* **2015**, *137*, 6097.
- [94] A. R. Carvalho, J. H. Warnes, C. H. Lewenkopf, *Phys. Rev. B* **2014**, *89*, 245444.
- [95] J. M. Cai, C. A. Pignedoli, L. Talirz, P. Ruffieux, H. Söde, L. B. Liang, V. Meunier, R. Berger, R. J. Li, X. L. Feng, K. Müllen, R. Fasel, *Nat. Nanotechnol.* **2014**, *9*, 896.
- [96] C. Bronner, S. Stremmlau, M. Gille, F. Brausse, A. Haase, S. Hecht, P. Tegeder, *Angew. Chem., Int. Ed.* **2013**, *52*, 4422.
- [97] Y. F. Zhang, Y. Zhang, G. Li, J. C. Lu, Y. D. Que, H. Chen, R. Berger, X. L. Feng, K. Müllen, X. Lin, Y. Y. Zhang, S. X. Du, S. T. Pantelides, H. J. Gao, *Nano Res.* **2017**, *10*, 3377.
- [98] Y. Cao, J. Qi, Y. F. Zhang, L. Huang, Q. Zheng, X. Lin, Z. H. Cheng, Y. Y. Zhang, X. L. Feng, S. X. Du, S. T. Pantelides, H. J. Gao, *Nano Res.* **2018**, *11*, 6190.
- [99] R. A. Durr, D. Haberer, Y. L. Lee, R. Blackwell, A. M. Kalayjian, T. Marangoni, J. Ihm, S. G. Louie, F. R. Fischer, *J. Am. Chem. Soc.* **2018**, *140*, 807.
- [100] S. Kawai, S. Saito, S. Osumi, S. Yamaguchi, A. S. Foster, P. Spijker, E. Meyer, *Nat. Commun.* **2015**, *6*, 8098.
- [101] G. D. Nguyen, F. M. Tom, T. Cao, Z. Pedramrazi, C. Chen, D. J. Rizzo, T. Joshi, C. Bronner, Y. C. Chen, M. Favaro, S. G. Louie, F. R. Fischer, M. F. Crommie, *J. Phys. Chem. C* **2016**, *120*, 2684.
- [102] S. Kawai, S. Nakatsuka, T. Hatakeyama, R. Pawlak, T. Meier, J. Tracey, E. Meyer, A. S. Foster, *Sci. Adv.* **2018**, *4*, eaar7181.
- [103] R. R. Cloke, T. Marangoni, G. D. Nguyen, T. Joshi, D. J. Rizzo, C. Bronner, T. Cao, S. G. Louie, M. F. Crommie, F. R. Fischer, *J. Am. Chem. Soc.* **2015**, *137*, 8872.
- [104] Z. Pedramrazi, C. Chen, F. Zhao, T. Cao, G. D. Nguyen, A. A. Omrani, H.-Z. Tsai, R. R. Cloke, T. Marangoni, D. J. Rizzo, T. Joshi, C. Bronner, W.-W. Choi, F. R. Fischer, S. G. Louie, M. F. Crommie, *Nano Lett.* **2018**, *18*, 3550.
- [105] B. V. Senkovskiy, D. Y. Usachov, A. V. Fedorov, T. Marangoni, D. Haberer, C. Tresca, G. Profeta, V. Caciuc, S. Tsukamoto, N. Atodiresei, N. Ehlen, C. Chen, J. Avila, M. C. Asensio, A. Y. Varykhalov, A. Nefedov, C. Woll, T. K. Kim, M. Hoesch, F. R. Fischer, A. Gruneis, *ACS Nano* **2018**, *12*, 7571.
- [106] Y. Fu, H. Yang, Y. Gao, L. Huang, R. Berger, J. Liu, H. Lu, Z. Cheng, S. Du, H.-J. Gao, X. Feng, *Angew. Chem., Int. Ed.* **2020**, *59*, 8873.
- [107] H. Hayashi, J. Yamaguchi, H. Jippo, R. Hayashi, N. Aratani, M. Ohfuchi, S. Sato, H. Yamada, *ACS Nano* **2017**, *11*, 6204.
- [108] E. Carbonell-Sanroma, J. Hieulle, M. Vilas-Varela, P. Brandimarte, M. Iraola, A. Barragan, J. Li, M. Abadia, M. Corso, D. Sanchez-Portal, D. Pena, J. I. Pascual, *ACS Nano* **2017**, *11*, 7355.
- [109] B. V. Senkovskiy, A. V. Fedorov, D. Haberer, M. Farjam, K. A. Simonov, A. B. Preobrajenski, N. Mårtensson, N. Atodiresei, V. Caciuc, S. Blugel, A. Rosch, N. I. Verbitskiy, M. Hell, D. V. Evtushinsky, R. German, T. Marangoni, P. H. M. van Loosdrecht, F. R. Fischer, A. Gruneis, *Adv. Electron. Mater.* **2017**, *3*, 1600490.
- [110] P. H. Jacobse, A. Kimouche, T. Gebraad, M. M. Ervasti, J. M. Thijssen, P. Liljeroth, I. Swart, *Nat. Commun.* **2017**, *8*, 119.
- [111] G. D. Nguyen, H.-Z. Tsai, A. A. Omrani, T. Marangoni, M. Wu, D. J. Rizzo, G. F. Rodgers, R. R. Cloke, R. A. Durr, Y. Sakai, F. Liou, A. S. Aikawa, J. R. Chelikowsky, S. G. Louie, F. R. Fischer, M. F. Crommie, *Nat. Nanotechnol.* **2017**, *12*, 1077.
- [112] D. J. Rizzo, M. Wu, H.-Z. Tsai, T. Marangoni, R. A. Durr, A. A. Omrani, F. Liou, C. Bronner, T. Joshi, G. D. Nguyen, G. F. Rodgers, W.-W. Choi, J. H. Jørgensen, F. R. Fischer, S. G. Louie, M. F. Crommie, *Nano Lett.* **2019**, *19*, 3221.
- [113] J. C. Li, N. Merino-Diez, E. Carbonell-Sanroma, M. Vilas-Varela, D. G. de Oteyza, D. Pena, M. Corso, J. I. Pascual, *Sci. Adv.* **2018**, *4*, eaaq0582.
- [114] T. Marangoni, D. Haberer, D. J. Rizzo, R. R. Cloke, F. R. Fischer, *Chem. - Eur. J.* **2016**, *22*, 13037.



- [115] X. L. Su, Z. J. Xue, G. Li, P. Yu, *Nano Lett.* **2018**, *18*, 5744.
- [116] O. Gröning, S. Wang, X. Yao, C. A. Pignedoli, G. Borin Barin, C. Daniels, A. Cupo, V. Meunier, X. Feng, A. Narita, K. Müllen, P. Ruffieux, R. Fasel, *Nature* **2018**, *560*, 209.
- [117] D. J. Rizzo, G. Veber, T. Cao, C. Bronner, T. Chen, F. Zhao, H. Rodriguez, S. G. Louie, M. F. Crommie, F. R. Fischer, *Nature* **2018**, *560*, 204.
- [118] H. Huang, D. Wei, J. Sun, S. L. Wong, Y. P. Feng, A. H. C. Neto, A. T. S. Wee, *Sci. Rep.* **2012**, *2*, 983.
- [119] A. Basagni, F. Sedona, C. A. Pignedoli, M. Cattelan, L. Nicolas, M. Casarin, M. Sambi, *J. Am. Chem. Soc.* **2015**, *137*, 1802.
- [120] T. Dienel, S. Kawai, H. Sode, X. L. Feng, K. Müllen, P. Ruffieux, R. Fasel, O. Groning, *Nano Lett.* **2015**, *15*, 5185.
- [121] S. Wang, N. Kharche, E. Costa Girão, X. Feng, K. Müllen, V. Meunier, R. Fasel, P. Ruffieux, *Nano Lett.* **2017**, *17*, 4277.
- [122] C. Ma, L. Liang, Z. Xiao, A. A. Puzetzy, K. Hong, W. Lu, V. Meunier, J. Bernholc, A. P. Li, *Nano Lett.* **2017**, *17*, 6241.
- [123] N. Merino-Diez, A. Garcia-Lekue, E. Carbonell-Sanroma, J. C. Li, M. Corso, L. Colazzo, F. Sedona, D. Sanchez-Portal, J. I. Pascual, D. G. de Oteyza, *ACS Nano* **2017**, *11*, 11661.
- [124] K. Sun, P. Ji, J. Zhang, J. Wang, X. Li, X. Xu, H. Zhang, L. Chi, *Small* **2019**, *15*, 1804526.
- [125] G. Calogero, N. R. Papior, B. Kretz, A. Garcia-Lekue, T. Frederiksen, M. Brandbyge, *Nano Lett.* **2019**, *19*, 576.
- [126] D. Beyer, S. Wang, C. A. Pignedoli, J. Melidonie, B. Yuan, C. Li, J. Wilhelm, P. Ruffieux, R. Berger, K. Müllen, R. Fasel, X. Feng, *J. Am. Chem. Soc.* **2019**, *141*, 2843.
- [127] H. J. Dai, *Acc. Chem. Res.* **2002**, *35*, 1035.
- [128] X. S. Li, W. W. Cai, J. H. An, S. Kim, J. Nah, D. X. Yang, R. Piner, A. Velamakanni, I. Jung, E. Tutuc, S. K. Banerjee, L. Colombo, R. S. Ruoff, *Science* **2009**, *324*, 1312.
- [129] Z. Chen, R. Berger, K. Müllen, A. Narita, *Chem. Lett.* **2017**, *46*, 1476.
- [130] R. Saito, M. Furukawa, G. Dresselhaus, M. S. Dresselhaus, *J. Phys.: Condens. Matter* **2010**, *22*, 334203.
- [131] J. Zhou, J. Dong, *Appl. Phys. Lett.* **2007**, *91*, 173108.
- [132] G. Borin Barin, A. Fairbrother, L. Rotach, M. Bayle, M. Paillet, L. Liang, V. Meunier, R. Hauert, T. Dumsloff, A. Narita, K. Müllen, H. Sahabudeen, R. Berger, X. Feng, R. Fasel, P. Ruffieux, *ACS Appl. Nano Mater.* **2019**, *2*, 2184.
- [133] D. Prezzi, D. Varsano, A. Ruini, A. Marini, E. Molinari, *Phys. Rev. B* **2008**, *77*, 041404.
- [134] K. Nakada, M. Fujita, G. Dresselhaus, M. S. Dresselhaus, *Phys. Rev. B* **1996**, *54*, 17954.
- [135] Y. W. Son, M. L. Cohen, S. G. Louie, *Nature* **2006**, *444*, 347.
- [136] W. Kim, K. Kim, *Nat. Nanotechnol.* **2008**, *3*, 408.
- [137] X. Wang, Y. Ouyang, X. Li, H. Wang, J. Guo, H. Dai, *Phys. Rev. Lett.* **2008**, *100*, 206803.
- [138] A. N. Abbas, G. Liu, A. Narita, M. Orosco, X. L. Feng, K. Müllen, C. W. Zhou, *J. Am. Chem. Soc.* **2014**, *136*, 7555.
- [139] P. Fantuzzi, L. Martini, A. Candini, V. Corradini, U. del Pennino, Y. Hu, X. Feng, K. Müllen, A. Narita, M. Affronte, *Carbon* **2016**, *104*, 112.
- [140] J. Gao, F. J. Uribe-Romo, J. D. Saathoff, H. Arslan, C. R. Crick, S. J. Hein, B. Itin, P. Clancy, W. R. Dichtel, Y. L. Loo, *ACS Nano* **2016**, *10*, 4847.
- [141] U. Zschieschang, H. Klauk, I. B. Mueller, A. J. Strudwick, T. Hintermann, M. G. Schwab, A. Narita, X. L. Feng, K. Müllen, R. T. Weitz, *Adv. Electron. Mater.* **2015**, *1*, 1400010.
- [142] R. Konnerth, C. Cervetti, A. Narita, X. Feng, K. Müllen, A. Hoyer, M. Burghard, K. Kern, M. Dressel, L. Bogani, *Nanoscale* **2015**, *7*, 12807.
- [143] P. B. Bennett, Z. Pedramrazi, A. Madani, Y. C. Chen, D. G. de Oteyza, C. Chen, F. R. Fischer, M. F. Crommie, J. Bokor, *Appl. Phys. Lett.* **2013**, *103*, 253114.
- [144] J. P. Llinas, A. Fairbrother, G. Borin Barin, W. Shi, K. Lee, S. Wu, B. Yong Choi, R. Braganza, J. Lear, N. Kau, W. Choi, C. Chen, Z. Pedramrazi, T. Dumsloff, A. Narita, X. Feng, K. Müllen, F. Fischer, A. Zettl, P. Ruffieux, E. Yablonovitch, M. Crommie, R. Fasel, J. Bokor, *Nat. Commun.* **2017**, *8*, 633.
- [145] M. C. Chong, N. Afshar-Imani, F. Scheurer, C. Cardoso, A. Ferretti, D. Prezzi, G. Schull, *Nano Lett.* **2018**, *18*, 175.
- [146] N. Richter, Z. Chen, A. Tries, T. Prechtel, A. Narita, K. Müllen, K. Asadi, M. Bonn, M. Kläui, *Sci. Rep.* **2020**, *10*, 1988.
- [147] A. Tries, N. Richter, Z. Chen, A. Narita, K. Müllen, H. I. Wang, M. Bonn, M. Klauk, *Phys. Chem. Chem. Phys.* **2020**, *22*, 5667.
- [148] A. Candini, L. Martini, Z. Chen, N. Mishra, D. Convertino, C. Coletti, A. Narita, X. Feng, K. Müllen, M. Affronte, *J. Phys. Chem. C* **2017**, *121*, 10620.
- [149] T. Mueller, F. Xia, P. Avouris, *Nat. Photonics* **2010**, *4*, 297.
- [150] L. Martini, Z. Chen, N. Mishra, G. B. Barin, P. Fantuzzi, P. Ruffieux, R. Fasel, X. Feng, A. Narita, C. Coletti, K. Müllen, A. Candini, *Carbon* **2019**, *146*, 36.
- [151] A. Candini, N. Richter, D. Convertino, C. Coletti, F. Balestro, W. Wernsdorfer, M. Klauk, M. Affronte, *Beilstein J. Nanotechnol.* **2015**, *6*, 711.
- [152] A. D. Franklin, *Nature* **2013**, *498*, 443.
- [153] B. L. Liu, F. Q. Wu, H. Gui, M. Zheng, C. W. Zhou, *ACS Nano* **2017**, *11*, 31.
- [154] X.-Y. Wang, M. Richter, Y. He, J. Björk, A. Riss, R. Rajesh, M. Garnica, F. Hennersdorf, J. J. Weigand, A. Narita, R. Berger, X. Feng, W. Auwärter, J. V. Barth, C.-A. Palma, K. Müllen, *Nat. Commun.* **2017**, *8*, 1948.
- [155] I. Piskun, R. Blackwell, J. Jornet-Somoza, F. Zhao, A. Rubio, S. G. Louie, F. R. Fischer, *J. Am. Chem. Soc.* **2020**, *142*, 3696.
- [156] Y. F. Li, Z. Zhou, C. R. Cabrera, Z. F. Chen, *Sci. Rep.* **2013**, *3*, 2030.
- [157] Y. Wang, Y. Li, *Theor. Chem. Acc.* **2014**, *133*, 1548.



**Zongping Chen** received his Bachelor's degree from Central South University in 2007, and then joined the group of Professor Hui-Ming Cheng at the Institute of Metal Research, Chinese Academy of Sciences as a graduate student, receiving his Ph.D. degree in 2013. Then he joined the group of Professor Klaus Müllen at Max Planck Institute for Polymer Research (MPIP) for postdoctoral research. In 2018, he joined Zhejiang University as a research professor. His current research focuses on the CVD synthesis of graphene and other 2D materials and their applications in composites, energy storage, electronic devices, etc.



**Akimitsu Narita** studied chemistry at the University of Tokyo, where he received his bachelor's (2008) and master's (2010) degrees under the supervision of Professor Eiichi Nakamura. He then joined the group of Professor Klaus Müllen at MPIP, and obtained his Ph.D. in chemistry in 2014, granted by the Johannes Gutenberg University of Mainz. Since 2014, he has been a group leader at MPIP. In 2018, he joined the Okinawa Institute of Science and Technology Graduate University (OIST) as an assistant professor (adjunct) and became assistant professor in 2020, leading the Organic and Carbon Nanomaterials Unit. His current research focuses on the bottom-up synthesis of functional nanocarbon materials, especially nanographenes and graphene nanoribbons, with atomically precise chemical structures.



**Klaus Müllen** studied chemistry at the University of Cologne and received his Ph.D. from the University of Basel in 1971. After postdoctoral research and his habilitation at ETH Zurich, he joined the University of Cologne as a professor in 1979 and moved to the University of Mainz in 1984. From 1989 to 2016, he was Director of the Synthetic Chemistry Department at MPIP. Since 2016, he has been an emeritus director and the leader of an emeritus group at MPIP, as well as a Gutenberg research fellow at the Johannes Gutenberg University of Mainz. His current research focuses on synthetic macromolecular chemistry, supramolecular chemistry, and materials science.